Master Thesis

Towards Radiation Tolerant Materials: Evaluation of Radiation Effects in interface-rich, nanostructured Cu-Fe-Ag

Michael Wurmshuber

This work has been carried out as a cooperation of the Department of Materials Physics at Montanuniversität Leoben and the Department of Nuclear Engineering at University of California, Berkeley.

Affidavit

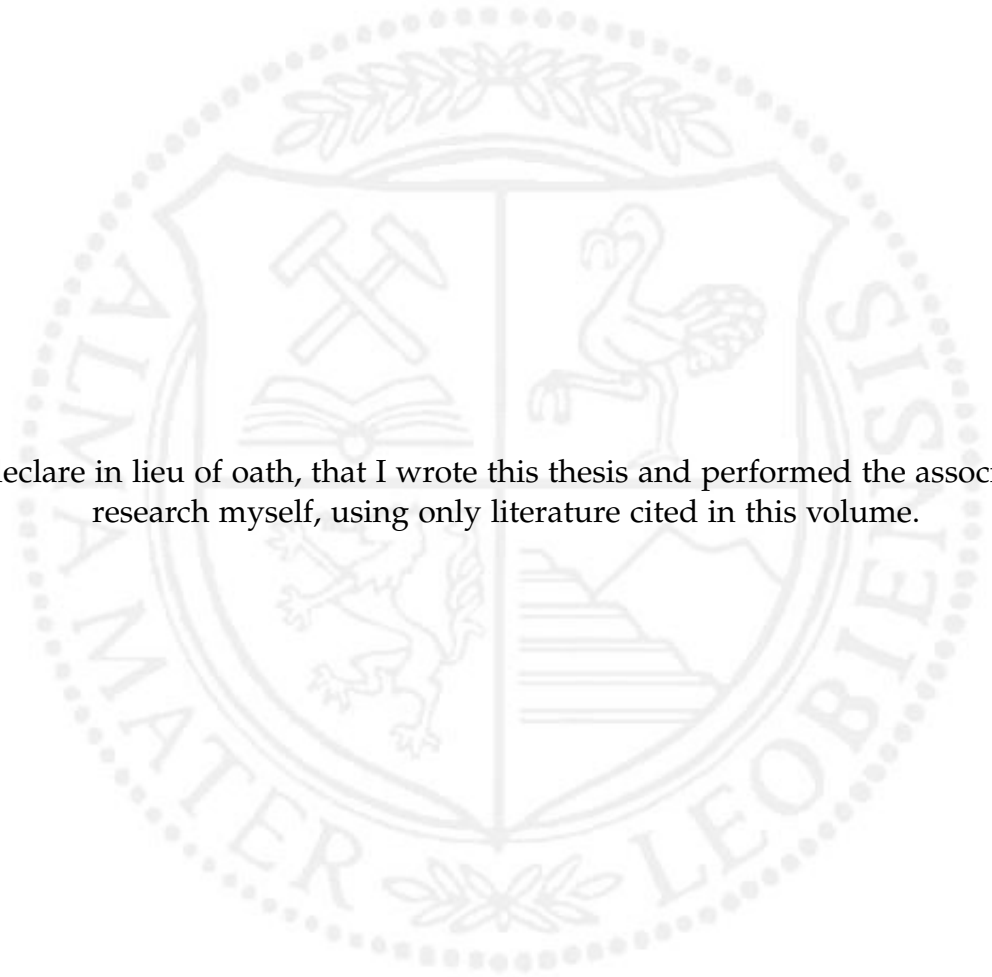

I declare in lieu of oath, that I wrote this thesis and performed the associated research myself, using only literature cited in this volume.

Place, Date	Michael Wurmshuber

Acknowledgements

I wish to express my profound gratitude to my advisor Assoc. Prof. Dr. Daniel Kiener for giving me the opportunity to write this thesis at the Department of Materials Physics in Leoben. I am very grateful for his guidance and counsel throughout the work. He always gave me excellent support, advice and constructive criticism and introduced me to the world of academic work and research.
In addition I want to thank Assoc. Prof. Dr. Peter Hosemann for making my research stay at the Department of Nuclear Engineering in Berkeley possible and providing the necessary research facilities. His scientific support and help with the proton irradiation is greatly acknowledged.

I am highly thankful to David Frazer M.S. for his support with the nanoindenter and helium implantations. The discussions with him were much appreciated and he ensured a smooth workflow during my time at Berkeley.
I am obliged to Dr. Andrea Bachmaier for sharing her know-how regarding sample fabrication. I am grateful for her cooperation during the period of my thesis.
My sincere thanks also goes to Dr. Jie Yang and Dr. Mehdi Balooch for their technical support regarding electrochemical experiments and AFM measurements.
I am thankful to Dr. Alexander Leitner for his help with conducting and analyzing additional nanoindentation experiments in Leoben.

I would like to express my great appreciation to my office colleagues in Leoben as well as Berkeley for the fruitful discussions and the positive and friendly atmosphere at both offices.
Furthermore, I want to thank my parents for all the support they have been giving me, as well as my sister Sandra and my closest friends.

A special mention goes to Hannah, greatly missed, who always believed in me.

Abstract

Newest developments in nuclear fission and fusion technology as well as planned long distance space missions demand novel materials to withstand harsh, irradiative environments. The main challenges for materials deployed in these applications are radiation-induced hardening and embrittlement as well as material swelling. The here underlying mechanisms are accommodation and clustering of lattice defects created by the incident radiation particles. Interfaces, such as free surface and phase boundaries, are known for trapping and annihilating defects and therefore preventing these radiation-induced defects from forming clusters.
In this work, nanocomposites of different grain size out of Cu-Fe-Ag were fabricated using mechanical alloying via High Pressure Torsion. Additionally, a nanoporous material was produced using electrochemical dealloying. The impact of a proton- and a helium-ion irradiation treatment on the mechanical properties of the differently structured samples was investigated via nanoindentation. The influence of the helium-ion dose on the swelling behavior of the material was characterized using atomic force microscopy.
The investigated interface-rich nanocomposites were proven to show tolerance against proton-irradiation damage. The bulk materials showed a slight decrease in hardness after irradiation, whereas the properties of the nanoporous material remain mostly unchanged. Extensive helium-ion implantation leads to bubble formation within the material and in further consequence to notable swelling and a foam-like behavior of mechanical properties. Depending on the helium dose and the interface-spacing in the material, different helium-bubble formation mechanisms were found to be dominant. The observed dose dependency of both, the swelling and the mechanical properties, for ultra-fine grained and nanocrystalline material can be explained by the bubble formation and -growth model proposed in this work.

Zusammenfassung

Neueste Entwicklungen in Kernspaltungs- und Kernfusionstechnologie, sowie geplante Langstrecken-Weltraummissionen verlangen nach neuartigen Materialien, die den dort vorherrschenden Belastungen standhalten. Die größte Herausforderung für Werkstoffe, die hier Anwendung finden, sind strahlungsinduzierte Härtung und Versprödung, sowie Anschwellen des Materials. Die grundlegenden Mechanismen hierfür sind Ein- und Zusammenlagerung von Gitterdefekten, die durch die einfallenden Strahlungsteilchen generiert werden. Grenzflächen, wie zum Beispiel freie Oberflächen oder Phasengrenzen, sind bekannt dafür Gitterdefekte einzufangen und auszulöschen und dadurch die Bildung von Defekt-Clustern zu verhindern.
In dieser Arbeit wurden Nanokomposite von unterschiedlicher Korngröße aus Cu-Fe-Ag durch mechanisches Legieren mit Hochdrucktorsionsverformung hergestellt. Zusätzlich wurden nanoporöse Proben durch elektrochemisches Ätzen gefertigt. Der Einfluss von Protonen- und Helium-Ionenbestrahlung auf die mechanischen Eigenschaften der unterschiedlich strukturierten Materialien wurde durch Nanoindentation untersucht. Die Auswirkung von verschiedenen Helium-Dosen auf das Schwellverhalten der Proben wurde mittels Rasterkraftmikroskopie gemessen.
Den untersuchten Nanokompositen konnte Toleranz gegen Protonen-Strahlungsschäden nachgewiesen werden. Die Massivmaterialien zeigten eine leichte Abnahme in Härte nach der Bestrahlung, während die Eigenschaften des nanoporösen Werkstoffs größtenteils unverändert blieben. Bestrahlung mit Helium-Ionen führt zu Blasenbildung innerhalb des Werkstoffs und in weiterer Folge zu beträchtlichem Anschwellen und einem schaumartigen Verhalten der mechanischen Eigenschaften. Es stellte sich heraus, dass, je nach Helium-Dosis und Grenzflächenabstand, unterschiedliche Mechanismen die Heliumblasenbildung dominieren. Die beobachtete Dosisabhängigkeit der mechanischen Eigenschaften sowie des Anschwellens von ultra-feinkörnigem und nanokristallinem Material kann auf das hier vorgestellte Modell für Blasenbildung und -wachstum zurückgeführt werden.

Abbreviations and Symbols

AFM	...	Atomic force microscopy
ARB	...	Accumulative Roll Bonding
at.%	...	Atomic percent
BCC	...	Body centered cubic
CG	...	Coarse-grained
CSM	...	Continuous stiffness measurement
DBTT	...	Ductile-brittle transition temperature
dpa	...	Displacements per atom
DSC	...	Differential scanning calorimetry
ECAP	...	Equal Channel Angular Pressing
EDX	...	Energy dispersive X-Ray spectroscopy
FCC	...	Face centered cubic
FIB	...	Focused Ion Beam
HCP	...	Hexagonal closed packed
HIP	...	Hot-isostatic pressing
HPT	...	High Pressure Torsion
ISE	...	Indentation size effect
K-P	...	Kinchin-Pease
LM	...	Light microscope
NC	...	Nanocrystalline
NP	...	Nanoporous
OCP	...	Open-circuit potential
PKA	...	Primary knock-on atom
RT	...	Room temperature
SEM	...	Scanning electron microscope
SFT	...	Stacking fault tetrahedron
SPD	...	Severe Plastic Deformation
SPM	...	Scanning probe microscopy
SRIM	...	"Stopping Range of Ions in Matter"
TEM	...	Transmission electron microscope
UFG	...	Ultra-fine grained
wt.%	...	Weight percent

Content

1 Motivation

The performance of materials in irradiative environments remains of great interest to the scientific community, due to the numerous existing nuclear power plants, the ongoing development of new reactor concepts and the uprising of nuclear fusion technology. Moreover, the recent revival of manned spacecraft demands new structural materials to withstand high-energy solar radiation and cosmic rays over long periods of time in order to ensure safe and successful space travel in the future.
The primary causes for failure of materials exposed to radiation are swelling, hardening and embrittlement. This is crucial especially for nuclear reactor materials, as the "leak before break" concept is often not fulfilled, causing a reduced failure tolerance. The increase in hardness and strength comes along with reduced total elongation and fracture toughness and stems from a plethora of radiation-induced lattice defects, such as dislocation loops or voids. Another concern for materials deployed in nuclear energy facilities is the generation of helium, as it forms gas bubbles within the material that add to the radiation embrittlement.
Nanostructured materials, such as nanocomposites and nanoporous foam materials, are a promising approach to mitigate these radiation-induced mechanical property changes, as they contain a great number of close-spaced interfaces where the introduced lattice defects can migrate and annihilate. Additionally, stable interfaces are known for storing helium, resulting in delayed bubble formation.

In this work, interface-rich Cu-Fe-Ag nanocomposites as well as multiphased nanofoams, containing a vast amount of free surface and additional phase boundaries, are fabricated using a novel solid state route. Mechanical properties of the different materials are characterized before and after a proton-irradiation treatment via nanoindentation, whereas the effect of helium-implantation on these materials is investigated per atomic force microscopy and continuous stiffness measurement-nanoindentation.

The goal of this thesis is not only to evaluate radiation effects on the here investigated materials, but also to shed light on the underlying defect recovery mechanisms, thereby creating a foundation for future development of novel materials for deployment in nuclear fission and fusion systems as well as space travel applications.

2 Theoretical Background

2.1 Impact of radiation on matter

In order to gain understanding of the interaction of radiation with matter, this section gives a short overview of the basics of radiation materials science. After the principles and types of radiation are characterized, the effects of radiation on material properties are described. Finally, different strategies and material concepts to overcome these radiation-induced property changes are discussed as the motivation for this thesis is underlined.

2.1.1 Radiation science fundamentals

Radiation is a form of energy released by an atom, travelling through space as a particle and wave. Depending on which particle carries the energy, radiation is classified in the following main types:

Alpha particle radiation: The alpha particle consists of 2 protons and 2 neutrons and is therefore equivalent to a helium nucleus. It is commonly symbolized as α, α^{2+} or He^{2+}, representing the helium ion. The main source of alpha particles is the alpha decay, which is based on quantum tunneling and mainly observed in high-mass nuclides:

$$ {}^{A}_{Z}P \rightarrow {}^{A-4}_{Z-2}D + \alpha \tag{2.1} $$

where P represents the parent nuclide, D the daughter nuclide, A the mass number of the parent nuclide, Z the atomic number of the parent nuclide and α the alpha particle, i.e. the helium nucleus carrying the energy released by the decay. Alpha particles can also be generated in diverse nuclear fusion reactions. They carry an energy of several MeV, but they are absorbed rather easily, since they lose their kinetic energy quickly by ionizing and exciting atoms on their path through space and eventually gain two electrons, becoming a ${}^{4}_{2}He$ atom [1].

Beta particle radiation: Beta particles are high-energy, high-speed electrons or positrons. They are a type of ionizing radiation also called beta rays. Depending on whether the resulting beta particle is an electron or a positron, one distinguishes between two types of beta decay, namely β^- and β^+, respectively. The β^- decay is represented by a neutron-rich nuclide changing a neutron to a proton and emitting an electron and an antineutrino. A famous example for this kind of decay is the use of carbon-14 in the method of radiocarbon dating to determine the age of an object containing organic material:

$$^{14}_{6}C \rightarrow {}^{14}_{7}N + \beta^- + \bar{\nu} \tag{2.2}$$

where β^- represents the beta particle (i.e. electron) and $\bar{\nu}$ an antineutrino. The energies of beta particles are typically below 1 MeV [1,2].

Gamma radiation: Gamma rays are high energetic, ionizing electromagnetic waves with wavelengths of less than 10 pm. When a nuclide is left in an excited state, e.g. after it went through a different nuclear reaction, it will decay into its ground state by releasing the exciting energy in form of a photon:

$$^{A}_{Z}P^* \rightarrow {}^{A}_{Z}P + \gamma \tag{2.3}$$

where P^* represents the parent nuclide in an excited state, P the parent nuclide in ground state and γ the gamma particle, i.e. a photon. As is apparent from Equation 2.3, gamma decay causes no change in mass and atomic number of the respective nuclide [1,2].

Neutron radiation: Neutron radiation is present in nuclear fission reactors, as some nuclides produced by fission reactions are neutron-rich and decay by emitting a neutron, leaving a different isotope of the same parent nuclide:

$$^{A}_{Z}P \rightarrow {}^{A-1}_{Z}P^* + {}^{1}_{0}n \tag{2.4}$$

the remaining isotope $^{A-1}_{Z}P^*$ will most likely undergo gamma decay, while the emitted neutron $^{1}_{0}n$ contributes to the nuclear chain reaction [1].

Proton radiation: Proton-rich nuclides may decay by emitting a proton and leaving a daughter nuclide :

$$^{A}_{Z}P \rightarrow {}^{A-1}_{Z-1}D + {}^{1}_{1}p \tag{2.5}$$

The emitted proton $^{1}_{1}p$ can also be viewed as an ionized hydrogen atom H^+. Since protons carry a charge, they can easily be accelerated to high energies and find therefore application in various particle accelerators for nuclear research purposes [1].

(Heavy) Ion radiation: Refers to radiation of ions that are heavier than helium. A common application of heavy ion radiation is the Focused Ion Beam (FIB), where typically Ga^+ ions are used to machine material on the micro- and nanoscale.

The types used for the radiation effect study in this thesis are proton and He-ion radiation due to practical as well as application relevant reasons, as is further discussed in Section 2.4.

2.1.2 Radiation damage and effects on materials

All the radiation particles discussed above interact with materials in a similar fashion, as they introduce defects to the crystal lattice, with vacancies and self-interstitials (so-called Frenkel pairs) being the most common type to be produced (Figure 2.1). These defects produced by the irradiation of material are called radiation damage, whereas the resulting changes of certain material properties due to the introduced defects are referred to as radiation effects [3].

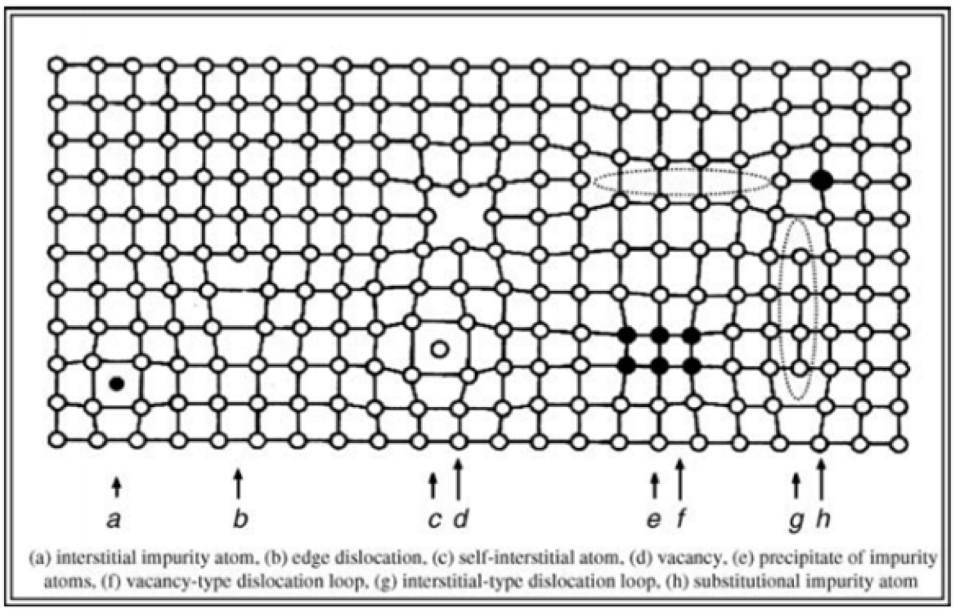

Figure 2.1 An overview of various types of radiation induced crystal defects. Self-interstitials (c) and vacancies (d) are most commonly found subsequent to material irradiation [3].

Radiation damage

The first interaction of an incoming radiation particle with the crystal lattice is called the radiation damage event and is divided into the following steps:

1. The incident particle interacts with a lattice atom.

2. Kinetic energy is transferred to the lattice atom $\rightarrow$ generation of the primary knock-on atom (PKA).

3. The PKA is displaced from its original lattice site.

4. The PKA is travelling through the lattice, producing more knock-on atoms in the process.

5. The above mentioned events eventually lead to a displacement cascade.

6. Finally, the PKA terminates as an interstitial.

The radiation damage event only takes about 10^{-11} seconds and leaves clusters of point defects in the material [4]. One of the first and simplest models to describe radiation damage was presented by Brinkman in 1956 [5]. This so-called displacement spike model suggests a core of vacancies along the path of the PKA, surrounded by an interstitial-rich area (see Figure 2.2).

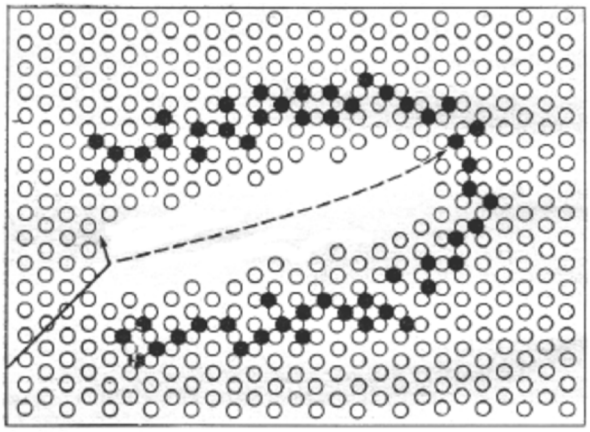

Figure 2.2 Displacement spike model by Brinkman [5]. The PKA creates a core of vacancies along its path (dashed line) which is surrounded by a periphery rich in interstitials (filled circles).

While this model is rather simplified and has later been refined, one can get an immediate idea that the depleted zone (the vacancy-rich area) can easily grow to voids when more vacancies are added, which leads to swelling of the material. The surrounding interstitials, however, can be imagined as obstacles for dislocation movement, leading to hardening and embrittlement.
A popular approach to estimate the amount of atomic displacements produced by a PKA with given energy is by using the Kinchin-Pease (K-P) model (see Figure 2.3) [6]. The K-P model is based on following assumptions:

- If the incident energy T is lower than a certain value called the displacement threshold E_d (~25 eV for most materials), no displacement of atoms occurs.
- When $E_d < T < 2E_d$, the PKA displaces a lattice atom but has an energy of less than E_d after the collision. The total amount of displacements is one.
- For $2E_d < T < E_c$, the displacements increase with increasing T, following $\frac{T}{2E_d}$.
- For high enough energies, the phenomenon of electronic stopping occurs. The incoming particle loses energy due to interactions with electrons until a certain cut-off energy E_c is reached. Thus, the number of displacements for $T > E_c$ remains constant at $\frac{E_c}{2E_d}$. E_c can be estimated to be the mass number of the radiation particle in keV, e.g. for protons $E_c \approx 1$ keV [7].

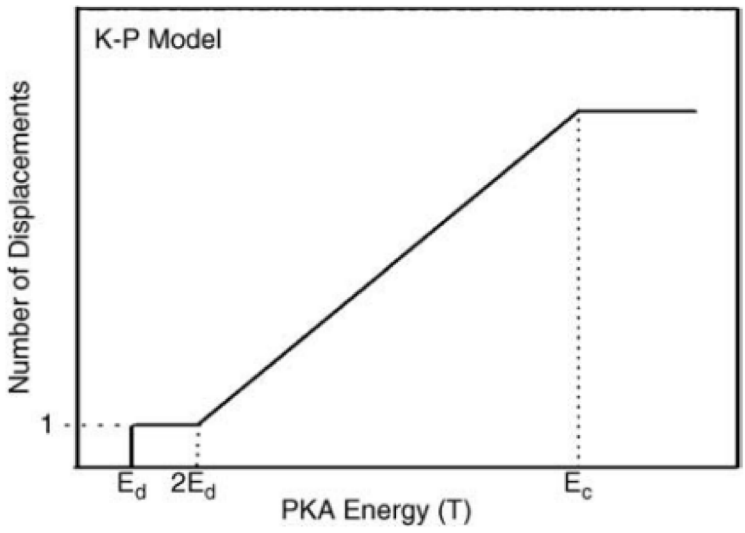

Figure 2.3 Amount of atoms displaced by a PKA with given energy according to Kinchin and Pease [6].

Radiation effects

Irradiation of material affects a variety of its properties. As this thesis is solely devoted to mechanical property changes and for the sake of clarity, this section will focus on radiation effects on mechanical material properties and the underlying mechanisms only.

A large portion of the Frenkel pairs produced by the radiation damage event recombine with each other or migrate to defect sinks to be annihilated right after they are formed. The remaining interstitials form clusters that eventually result in dislocation loops. Figure 2.4 shows such a dislocation loop (or Frank loop) with its screw components on the sides of the loop that are parallel to the burgers vector and the edge components on the sides that are perpendicular to it. Because the line senses of the segments facing each other are opposite, the whole loop is not able to move into the same direction when shear stress is applied. However, it can alter its radius and therefore grow or shrink, depending on the defect flux, and remains stable once it reaches a critical radius.

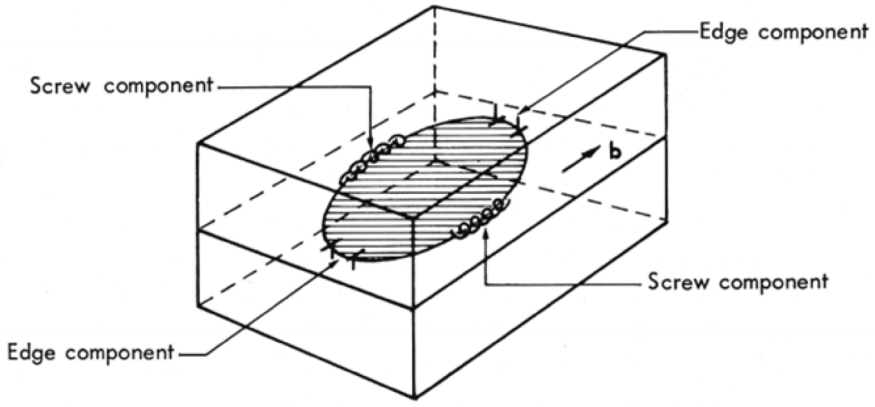

Figure 2.4 Dislocation loop formed due to interstitial movement and clustering [8].

Vacancies also tend to attract each other, but they diffuse slower than interstitials, as the bonding of interstitials is generally weaker and there are many more free interstitial sites than vacancy sites to jump to. They can agglomerate by either forming a vacancy-type dislocation loop or three-dimensional clusters called voids. Since dislocations in the material act as preferential interstitials sinks, the excess vacancies can not recombine, which leads to further growth of voids and eventually to void swelling of the material [3].

Another type of vacancy clusters that can form due to a vacancy supersaturation are so-called stacking fault tetrahedra (SFTs). The structure of these SFTs can be imagined in the following way: Take atoms surrounded by four {111} planes in the form of a tetrahedron (triangle-based pyramid) out of the crystal lattice. Remove one atomic layer of this tetrahedron and put it back in its original site by placing the center of the reduced tetrahedron into the center of the opening, thereby creating a stacking fault in each of the four {111} planes [9]. Depending on the point defect flux, SFTs tend to grow (absorption of vacancies) or shrink (absorption of interstitial atoms). The formation of SFTs is energetically more favorable in FCC metals with low stacking fault energy and is therefore often observed in irradiated gold, silver or copper. Nanostructured materials with close interface-spacing are also known to exhibit a great amount of SFTs or vacancy clusters in general, as the more mobile interstitials annihilate on these interfaces, leaving a vast amount of less mobile excess vacancies that eventually form voids, loops or SFTs [9,10].

Frank loops as well as voids and SFTs act as obstacles to dislocation movement in the material, which leads to an increase in strength and hardness but also a drastic decrease in ductility. This strengthening effect is also known as radiation hardening and can be observed in Figure 2.5 (a) for a low-alloy ferritic reactor pressure vessel steel. The higher the dose in terms of dpa (displacements per atom) gets, the harder and more brittle the material gets. The embrittling effect of radiation on a BCC alloy that exhibits a ductile-brittle transition temperature (DBTT) is depicted in Figure 2.5 (b). While the DBTT shifts to higher temperatures due to the radiation-induced defects, the upper shelf energy diminishes, which indicates a decreased fracture toughness [3].

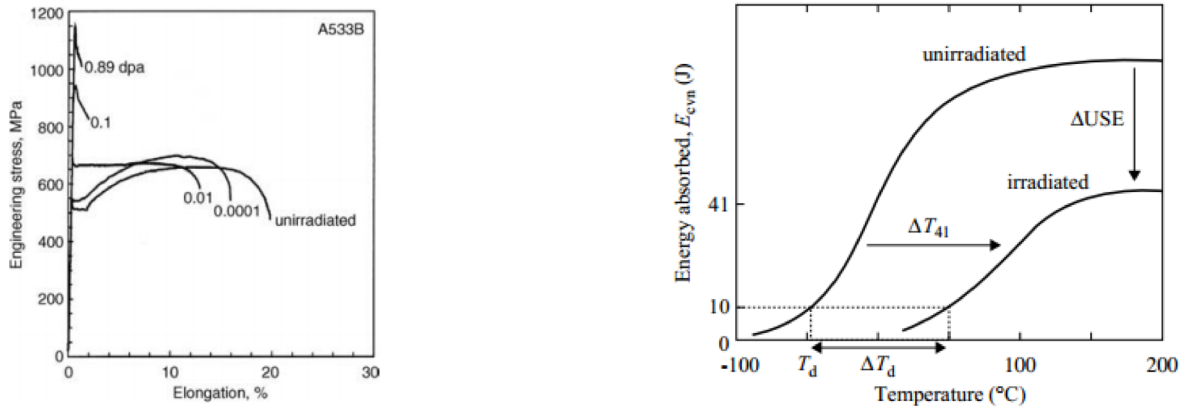

Figure 2.5 Radiation effects on mechanical properties. (a) Radiation hardening of an A533B reactor pressure vessel steel [11]. (b) Radiation embrittlement effects on materials that exhibit a DBTT [12].

For materials deployed in safety-relevant structural applications a reduction in ductility and fracture toughness is crucial, as material failure can lead to cost intensive or even fatal accidents. Therefore, materials exposed to irradiative environments, such as nuclear reactor materials or components for space travel applications, are desired to avoid, mitigate or even self heal these mechanical property changes in order to ensure a longer lifetime and a decreased safety risk.

2.1.3 Role of helium in nuclear materials

Another major challenge for materials deployed in nuclear fusion, fission or spallation systems is helium, which is generated from transmutation reactions inside the material (e.g. alpha decay). The solid solubility of He in metals is extremely low and therefore He tends to precipitate into gas bubbles within the material. These bubbles arrange themselves on a superlattice with respect to the host material lattice (see Figure 2.6) [13,14].

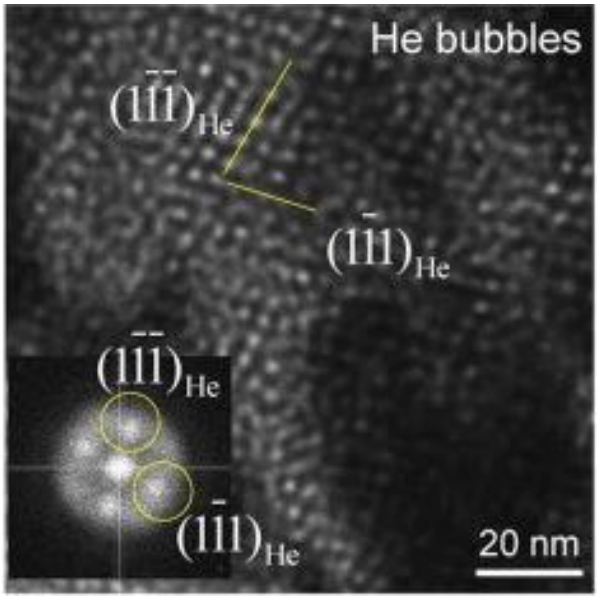

Figure 2.6 Helium gas-bubble superlattice in single-crystal copper. Inset: Fast Fourier Transformation of the He superlattice [14].

Gas bubbles act as additional dislocation barriers and facilitate intergranular cracking, which adds to the embrittling effect of the primary radiation. This embrittlement is not reversible, since annealing of the material leads to growth of the bubbles, reducing the ductility and fracture toughness even more. The cause of helium embrittlement is a widely studied topic and various theories have been developed, depending on where the helium bubbles accommodate themselves [7].

If the bubbles settle in the interior of the grain, the resulting stress concentrations at the grain boundaries cannot relax and cause cracks that run along the grain boundary. Helium bubbles accommodating on grain boundaries, however, will grow when stress is applied and eventually link up and lead to intergranular failure.
The effect of helium embrittlement is less pronounced in BCC metals, since the packing density is lower than in FCC or HCP metals and therefore the stress concentrations at the grain boundaries can relax more easily [3].
Since helium strongly interacts with vacancies to promote the formation of cavities, excess interstitial atoms cannot recombine, which leads to an increase in dislocation loop concentration in helium-containing materials [15].

2.1.4 Material concepts to reach enhanced radiation endurance

Various strategies and concepts to overcome radiation-induced mechanical property changes have been developed in recent years [16–22]. As defect accommodation is at the root of material embrittlement, the key to reach maximum radiation endurance is perfect defect recovery. This implies that the induced Frenkel pairs have to be annihilated faster than they are generated in order to avoid the above mentioned clustering and formation of voids or dislocation loops. In this section, two popular concepts of introducing defect sinks into materials are presented.

Metallic nanofoams

Nanoporous metal foams exhibit a high surface-to-volume ratio, low specific weight, high energy absorption and excellent thermal and electrical conductivity, which makes them suitable for various applications such as electrocatalysts, sensors, actuators, lightweight structures, dampeners and heat exchangers [23–26]. Extensive research has been performed in recent years to investigate the behavior of nanoporous materials under irradiation and it was found that the vast amount of free surface in these foams act as perfect defect sinks [18, 19, 22]. Molecular Dynamics simulations yielded that the recovery performance of the foam depends strongly on two parameters, (i) the size of the foam ligaments and (ii) the distance that the defects migrate in the time between radiation collision cascades. Using these findings, a window of radiation endurance in terms of dose rate and ligament diameter was proposed (Figure 2.7) [19]. Within this window, radiation induced defects migrate to the free surface and annihilate before the next collision cascade, therefore avoiding clustering and defect accommodation.

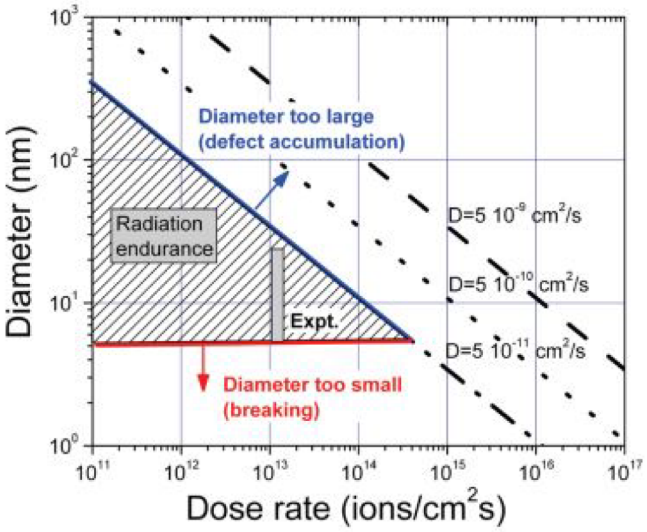

Figure 2.7 Window of radiation endurance for nanoporous Au [19].

Sun et al. [22] used in situ investigations to observe rapid annihilation of dislocation loops and removal of SFTs by free surface in nanoporous (NP) Ag. A defect gradient over the foam ligaments and several nm wide surface-affected-zones (SAZs) seem to be the cause of these findings. Additionally, the diffusivity of defect clusters in NP Ag was found to be lower than in coarse-grained (CG) Ag. This unexpected phenomenon can be explained by a smaller interaction energy of defect clusters in NP Ag, resulting in smaller attractive forces between these clusters and the average size of defect clusters being smaller. Hence, the stress fields generated by clusters are weaker and have larger spacing between them, allowing defects to migrate to free surface without getting trapped and contributing to cluster growth (Figure 2.8).

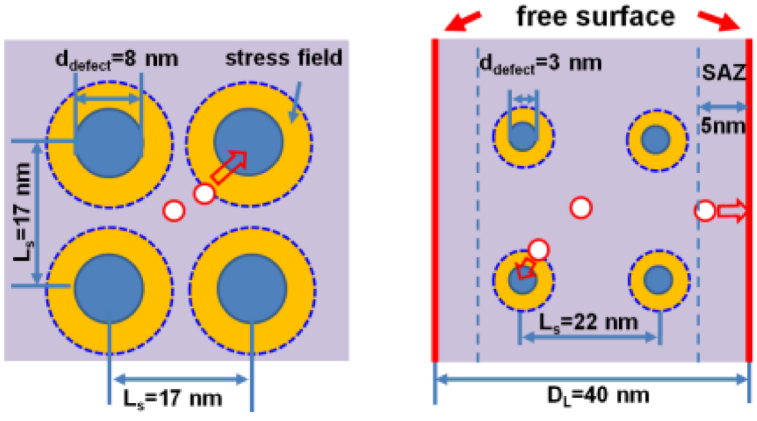

Figure 2.8 Schematic illustration of average cluster size and defect migration kinetics in (left) CG and (right) NP Ag [22].

Interface-rich nanocomposites

Aside from free surfaces, stable phase boundaries are another promising approach to trap defects. When the distance between these interfaces is reduced to the nanometer regime, as is the case for bulk nanocomposites (Figure 2.9 (a)), point defects are more likely to migrate to the nearby sinks. The interfaces in these materials are not only known for effectively trapping point defects (Figure 2.9 (b)), but also for storing helium, therefore delaying nucleation of He bubbles as well as retarding their growth [17].
Aside from their excellent defect recovery properties, nanolayered materials exhibit high hardness and strength and can be manufactured in large quantities using Accumulative Roll Bonding (described in Section 2.2.2), creating thermally stable interfaces in the process [21].

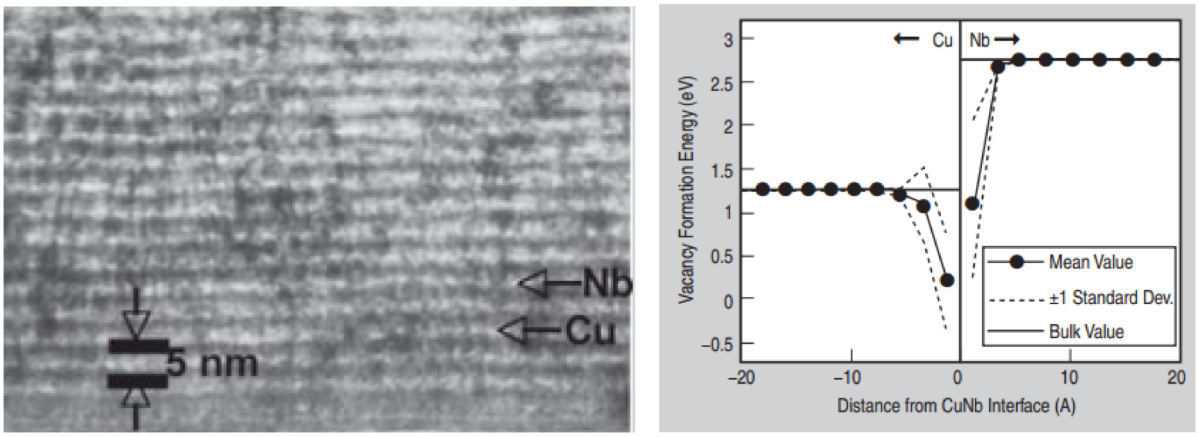

(a) **(b)**

Figure 2.9 Nanolayered bulk Cu-Nb containing stable phase boundaries. (a) Microstructure. (b) Simulated vacancy formation energy at interfaces [17].

In order to reach maximum radiation resistance it is nothing but logical to combine these two concepts by creating a nanoporous, polyphased material, leading to a vast amount of free surface with additional interfaces within the foam ligaments. It is the goal of this work to investigate the influence of different amounts and types of interfaces on radiation damage tolerance by comparing radiation effects on nanoporous (NP), ultra-fine grained (UFG) and nanocrystalline (NC) nanocomposites.

2.2 Material and fabrication processes

2.2.1 Material selection

The material selection for this work was driven by the demand for three components that are not soluble in each other in order to introduce phase boundaries in the material. As is apparent from the large miscibility gaps in the respective phase diagrams (Figure 2.10 (a)-(c)), this is the case for copper, iron and silver. At typical operating temperatures of about 320°C in pressurized water reactors, the solid solubility of these components is still negligibly small.

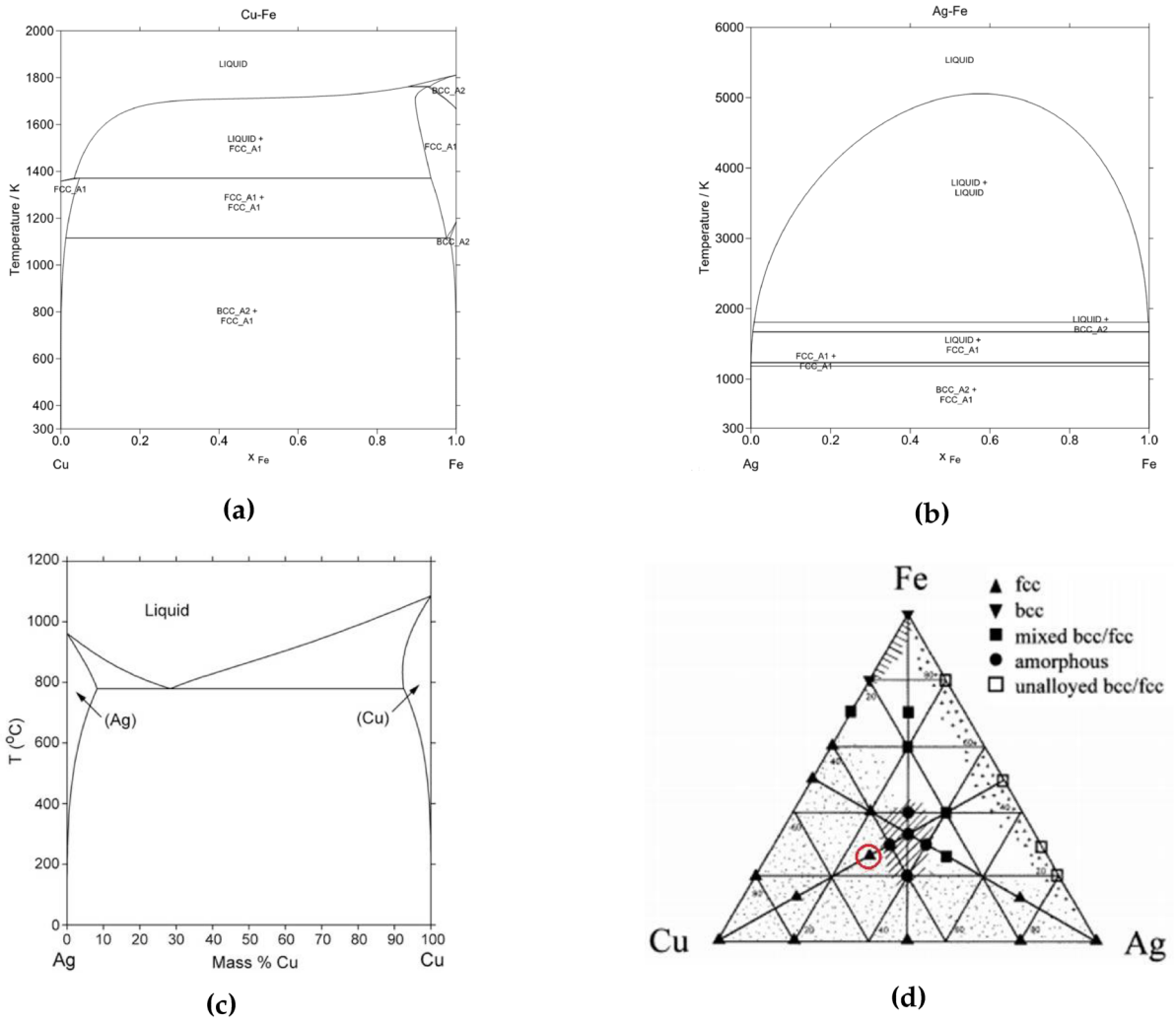

Figure 2.10 Phase diagrams of (a) Cu-Fe [27], (b) Ag-Fe [28] and (c) Ag-Cu [29] binary systems and (d) Cu-Fe-Ag ternary system [30].

Another asset that speaks for choosing the Cu-Fe-Ag ternary system is that it has already been investigated in terms of mechanical alloying [30, 31]. Figure 2.10 (d) shows the ternary phase diagram of the system and the resulting microstructure of different compositions after 70 hours of ball milling. The marked composition of $Cu_{50}Fe_{25}Ag_{25}$ showed the most promising results in earlier experiments conducted at the Department of Materials Physics in Leoben and was therefore chosen for this work.

2.2.2 Severe plastic deformation

Severe plastic deformation (SPD) is a popular approach for fabricating bulk UFG and NC materials, as it yields several advantages over other techniques, like no residual porosity as in nanopowder compacted samples or less impurities than in ball-milled samples. The immense deformation at typically low temperatures leads to an increase in dislocation density and vacancy concentration as well as to the formation of a vast amount of high angle grain boundaries and, hence, grain refinement. The microstructural changes induced by SPD come along with unique material properties. Aside from changes in magnetic, optical and elastic properties, enhanced diffusion and remarkable mechanical properties draw the interest of the scientific community to study SPD-fabricated UFG materials for various possible applications [32]. The most common SPD techniques: Equal Channel Angular Pressing (ECAP), Accumulative Roll Bonding (ARB) and High Pressure Torsion (HPT) are depicted in Figure 2.11.

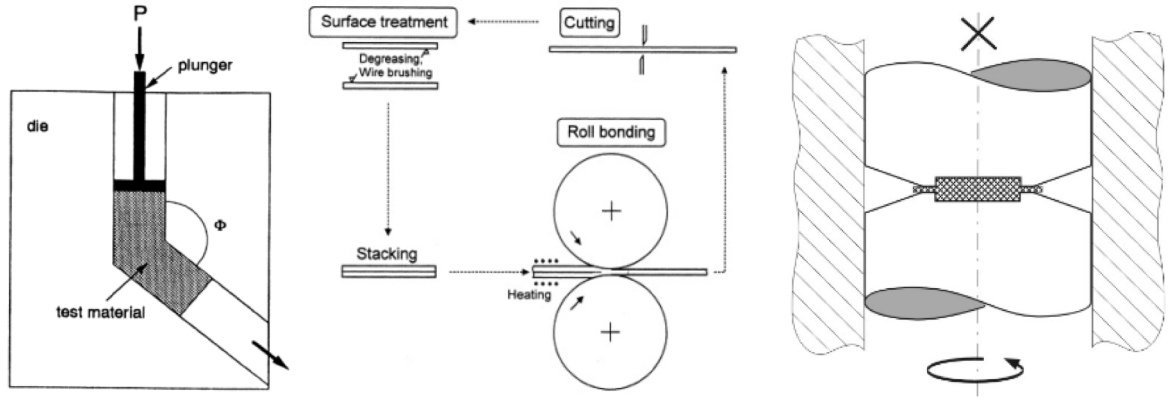

Figure 2.11 Most common SPD methods: (a) ECAP-Process [32], (b) ARB-Process [33] and (c) HPT-Process [34].

Figure 2.11 (a) shows the principle of ECAP, where material billets are pushed through a die consisting of two channels. These channels are equal in cross-section, which allows multiple passes of the billets. The amount of passes as well as the rotation of the material between passes and the angle Φ between the channels determine the amount of plastic shear deformation the material undergoes [32, 33, 35]. The ARB process can be seen in Figure 2.11 (b). A rolled sheet of metal is cut in half, degreased and then stacked together to be rolled again. This procedure is not only a deformation but also a bonding process and can be repeated limitlessly. A big asset of ARB is that it is able to fabricate large amounts of UFG material using conventional rolling facilities [33].
As HPT is the SPD method used in this work, it is explained in more detail in the next section.

High Pressure Torsion

As is apparent from Figure 2.11 (c), with HPT a disk-shaped sample is placed between two anvils and torsion-strained under high pressure of several GPa. Surface friction forces the material to be deformed by pure shear and due to the quasihydrostatic compression no cracks appear during deformation, making it also a suitable option for brittle materials.
The largest strain values of all SPD methods can be achieved with HPT. The imposed shear strain γ is calculated from the following equation:

$$\gamma = \frac{2\pi RN}{t} \tag{2.6}$$

where R is the radial position on the disk sample, N the number of rotations and t the sample thickness. To compare this shear strain to strain induced by other deformation processes, the equivalent Von Mises strain ε_{eq} can be calculated:

$$\varepsilon_{eq} = \frac{\gamma}{\sqrt{3}} \tag{2.7}$$

However, Equation 2.6 should be used for approximation only, as the initial thickness of the sample changes during the deformation process and therefore the strain is underestimated. It also indicates that the center of the sample is not influenced by the HPT process, yet experiments confirmed that there is also significant grain refinement at $R = 0$ mm due to non-perfect co-axiality of the anvils [32, 35].

Mechanical alloying via High Pressure Torsion

Recent studies used HPT to mechanically alloy a variety of immiscible systems, creating single-phased, metastable structures in the process [36–40]. While it is believed that the driving force for mixing in these systems is increased by the strong reduction in grain size and capillary pressure effects, the diffusion kinetics in SPD-processed materials are also improved by several orders of magnitude. High angle grain boundary diffusion and pipe diffusion along dislocations in these materials are accompanied by an increased vacancy concentration and mobility, which is believed to have a significant influence on the formation of non-equilibrium supersaturated solid solutions [36, 38]. A subsequent heat treatment can help the system to reach thermodynamic equilibrium once again by separating in its initial components. By adjusting temperature and time of the annealing process, grain growth and therefore the microstructure of the material can be controlled [31].

2.2.3 Selective dissolution

In order to create a NP foam out of the Cu-Fe-Ag alloy, selective dissolution seems the most convenient process. As demonstrated in previous works [41, 42], a combination of a noble element and iron can be turned into a foam material rather easily by free corrosion in hydrochloric acid (HCl). The choice of HCl as a dissolvent is also reasonable for the here investigated system, as it should dissolve iron but neither copper nor silver (Figure 2.12) [43].
However, failed foam processing experiments showed that selective dissolution of ternary alloys is not as trivial as is the case for binary systems, which is outlined in the next section.

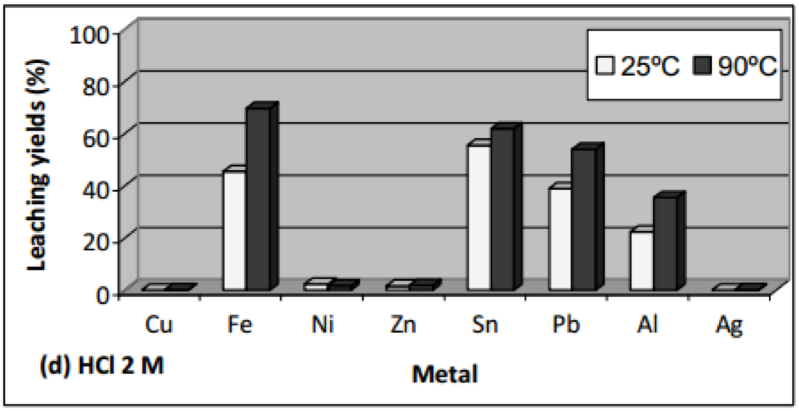

Figure 2.12 Leaching yields for different metals in 2 molaric HCl [43].

Electrochemical considerations

While selective dissolution experiments in Cu-Fe [41] and Au-Fe [42] alloys under free corrosion conditions yielded more or less iron-free nanoporous foams, similar experiments conducted with the Cu-Fe-Ag alloy during this work resulted in a coarsely porous material (Figure 2.13). Subsequent EDX analysis showed that not only the iron but also the copper dissolves, leaving a nearly pure silver foam. This indicates that the presence of a more noble element (i.e. silver) leads to a galvanic corrosion effect and therefore the dissolution of Cu.

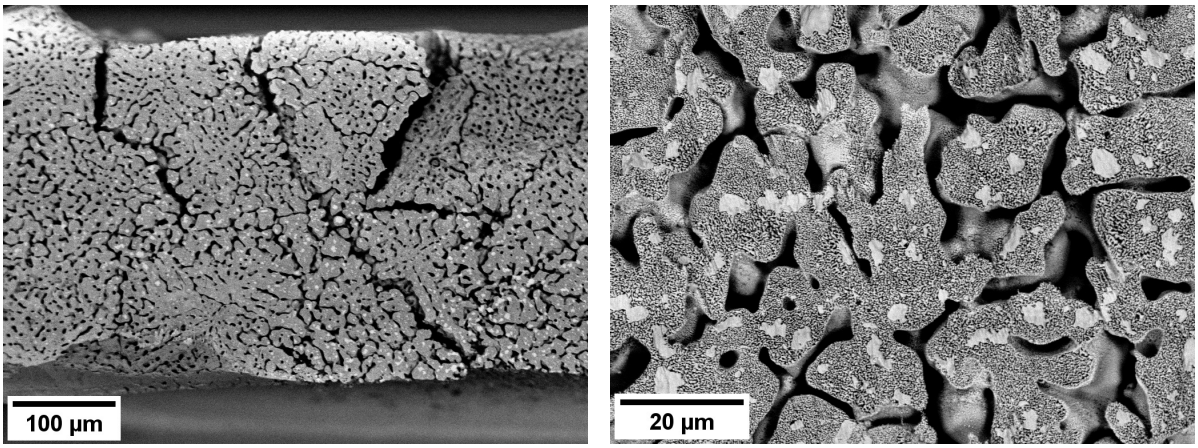

(a) **(b)**

Figure 2.13 SEM images (back scattered electron mode) of the coarsely porous microstructure after free corrosion of Cu-Fe-Ag in 2 molaric HCl for 24 hours at 55°C. (a) Microstructure with low magnification and (b) higher magnification.

While the standard electrode potentials of the most common dissolution reactions for the three elements (see Table 2.1) indicate that there is a large difference in the electrochemical potentials, one has to consider that this may not be the case in a different environment like a HCl solution. Moreover, the overall potential of a ternary alloy cannot be approximated that easily, especially if the material underwent such a complicated fabrication process and various metastable states beforehand.

Table 2.1 Standard electrode potentials at 298 K [44].

Half-reactions	**E°/V**
$Ag^+ + e^- \rightleftharpoons Ag$	+0.80
$Cu^{2+} + 2e^- \rightleftharpoons Cu$	+0.34
$Fe^{2+} + 2e^- \rightleftharpoons Fe$	-0.44

In order to overcome these difficulties, the open-circuit potential (OCP) of the alloy and its components has to be measured using a simple three-electrode setup connected to a potentiostat (Figure 2.14). A working electrode (i.e. the sample) is put into an electrochemical cell together with a counter electrode (usually Pt) and a reference electrode, while the desired etching solution serves as electrolyte. The potential of the sample with respect to the reference electrode is measured using the potentiostat and should get stable once the system reaches a quasidynamic equilibrium.

Potentiostatic dealloying

Once the potentials of the different components are determined, the selective dissolution process will not be conducted under free corrosion conditions but rather by using potentiostatic dealloying. This approach uses the same setup as seen in Figure 2.14, but this time the potentiostat is used to apply a voltage between the sample and the counter electrode. This voltage pushes the overall electrochemical potential of the system between the potentials of copper and iron, allowing copper to be protected and ensuring only dissolution of iron.

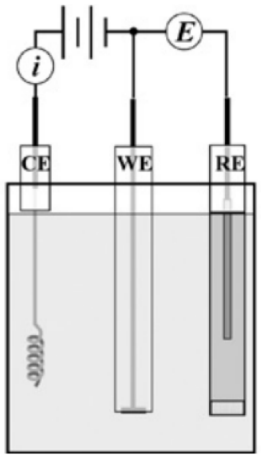

Figure 2.14 Schematic sketch of a three-electrode electrochemical cell with counter electrode (CE), working electrode (WE) and reference electrode (RE) [45].

2.3 Mechanical properties of porous materials

The mechanical behavior of three-dimensional foam materials differs from their bulk counterparts due to the unique structure. A schematic compressive stress-strain curve for an elastic-plastic foam is depicted in Figure 2.15. The first part of the curve shows a linear elastic region, mainly controlled by bending of cell walls, with the initial slope of the curve representing the Young's modulus. Once the yield strength σ^*_{pl} is reached, several foam ligaments experience plastic buckling, allowing large displacements at an almost constant stress level, resulting in a long collapse plateau in the curve. When all foam ligaments are collapsed and touching each other, densification occurs, leading to a rapid increase in flow stress. Depending on the porosity of the foam, the plateau stress and start of the densification may vary [46].

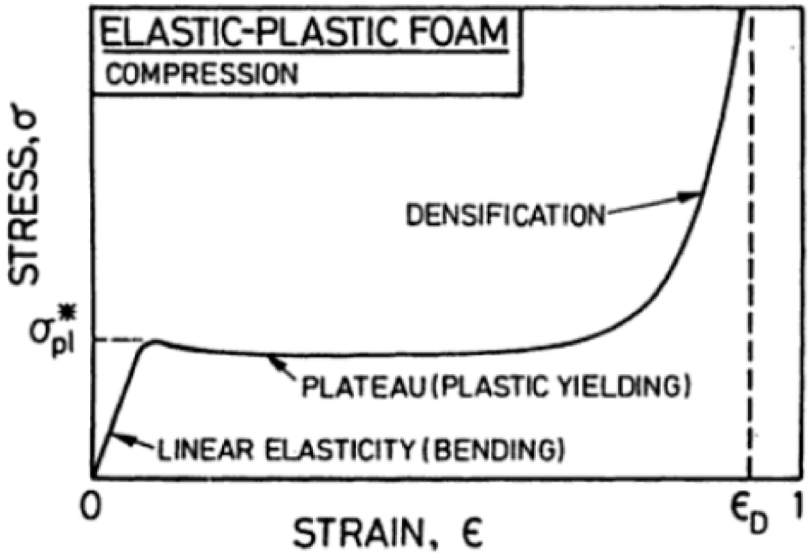

Figure 2.15 Schematic stress-strain curve during compression of an elastic-plastic metallic foam [46].

Gibson and Ashby [46] developed a relation between mechanical properties of macroscopic foams and bulk materials:

$$\sigma^*_y = C_1 \cdot \sigma_{y,s} \cdot \left(\frac{\rho^*}{\rho_s}\right)^m \tag{2.8}$$

$$E^* = C_2 \cdot E_s \cdot \left(\frac{\rho^*}{\rho_s}\right)^n \tag{2.9}$$

with $\sigma_{y,s}$ as the yield strength, E_s the Young's modulus and ρ_s the density of the solid bulk material and σ_y^* the yield strength, E^* the Young's modulus and ρ^* the density of the porous foam. The constants in these equations describe the cell geometry and cell deformation behavior and are well estimated for most foams with $C_1 = 0.3$, $C_2 = 1$, $m = 1.5$ and $n = 2$.
While the Equations 2.8 and 2.9 have been developed for macroscopic low-density foams, their validity for microscopic foams and NP materials is still under debate [47,48]. However, they can provide a first estimate of mechanical properties of NP materials.

The Poisson's ratio ν of NP materials is a highly discussed topic. While earlier studies assumed an uniaxial stress state in the ligaments and therefore $\nu = 0$ [47,49], several authors estimate a ratio of $\nu = 0.2$ [50,51]. An average value of 0.22 for ν was later confirmed by axial and transverse strain measurements on NP Au [48]. As to the best knowledge of the author there are no studies regarding the Poisson's ratio of multiphased NP materials and the here investigated material is expected to show lower porosity and bigger ligament diameters as the above studied foams, a value of 0.2 is assumed throughout this work.

2.4 Notes on material irradiation

While materials deployed in nuclear reactors are mainly exposed to neutron irradiation, the emulation of these conditions for research purposes is not a straightforward task to do.
The irradiation of material with neutrons comes along with a series of drawbacks. Due to the fact that a nuclear reactor is necessary to act as neutron source, neutron irradiation treatment is costly and can lead to problems regarding logistics, as not many such test reactors exist. Additionally, neutron irradiation is rather time-consuming as it operates at low dose rates (under 20 dpa/year) and is therefore slow to reach significant radiation damage, increasing the costs of the treatment even more. Furthermore, neutrons activate the material by triggering a variety of nuclear reactions. The handling of radioactive material in so-called hot cells is rather cumbersome and desirable to avoid [4,52].
Due to these disadvantages, alternative types of irradiation treatment have received a lot of attention lately. While electron irradiation has the advantage of being feasible in a conventional high voltage transmission electron microscope (TEM), its typically low energies (< 1 MeV) are not sufficient to produce a displacement cascade. Therefore the radiation damage is not comparable with damage caused by neutrons and electron irradiation is not further considered a suitable option [4].

Ion-beam irradiation, however, introduces significant radiation damage to materials in a relatively short amount of time, benefiting from a rather high dose rate (up to 100 dpa/day). As ion accelerator facilities act as the source, ion irradiation also offers easy access and good control of the experimental conditions. Additionally, when the energy of the ions is chosen beneath the Coulomb barrier, no activation of material occurs, making it much more convenient than handling radioactive samples produced by neutron irradiation. The biggest drawback of ion irradiation is that due to the charge of the ions, they lose their energy rather quickly as they interact with free electrons inside the material, leading to a small penetration depth (0.1 - 100 µm for usual accelerator energies) in contrast to charge-neutral neutrons (several mm). The penetration depth and dose profile for different ions and neutrons are depicted in Figure 2.16. From this graph one can immediately see that while neutrons have a relatively flat dose profile, ions exhibit what is called a stopping range peak near their final penetration depth. Within this stopping range most of the ions have lost their kinetic energy and settle down as interstitial atoms, which explains the increased displacement damage in this region. It is also apparent from Figure 2.16 that light ions show a larger penetration depth than heavy ions. This fact and their general availability make protons (H^+) a favorable choice for ions in irradiation experiments [4, 52–54].

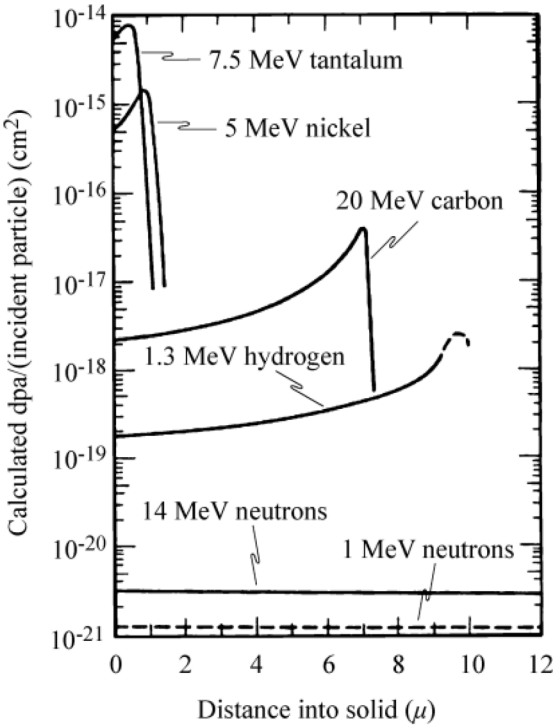

Figure 2.16 Penetration depth and dose profile of several ions and neutrons at different energies [4].

Was et al. [52] investigated the comparability of neutron and ion radiation damage on stainless steel. It was found that ion irradiation has to be conducted at higher temperatures to reach a similar damage microstructure than neutron irradiation. This is due to the fact that at higher dose rates more displacement cascades are introduced over a shorter period of time. In order to ensure these additional defects produced by ions can migrate and annihilate faster, temperature (and therefore diffusion) has to be increased to get comparable loop size distribution and loop densities as is the case for neutron irradiated material. Once these parameters are matched, radiation effects such as radiation hardening, radiation induced segregation or irradiation assisted stress corrosion cracking show similar results after either neutron or ion-beam irradiation on the same material.
The good agreement in these results as well as the overcoming of difficulties with neutron irradiation makes proton irradiation serve as state-of-the-art method for fundamental radiation damage studies and is therefore also used in this work.

While, in general, activation of materials is not desired due to the aforementioned reasons, the fact that helium is generated by transmutation reactions within radioactive samples can not be mimicked using proton irradiation. As the effect of He on material properties is of great interest to the nuclear community, samples are implanted with He using a helium-ion microscope within the scope of this work.

2.5 Challenges with irradiated materials testing

The limited penetration depth of ions makes the evaluation of radiation-induced mechanical property changes rather difficult. In order to make sure only material volume with significant radiation damage is tested, small-scale testing is inevitable. Another factor that speaks in favor of small-scale mechanical testing is that due to the limited space in a nuclear reactor, only limited amount of testing material is available. The necessity of collecting enough data points to reach the required statistical certainty, yet at the same time test as little material volume as possible, gave rise to small-scale testing as a promising tool for the safety-relevant evaluation of these control samples [53, 54].

As the need of small-scale methods arises, instrumented microhardness testing (nanoindentation) seems to be an excellent choice, since only little sample preparation is needed to gain insight in the mechanical behavior of the material. As it is also the method of choice in this thesis, nanoindentation and its role in irradiated materials testing is further described in the next section.

2.6 Nanoindentation

The method of nanoindentation is based on the principles of simple hardness testing, where an indenter out of a material of high hardness (e.g. diamond) is pushed into the specimen. The used load P_{max} together with the contact area between indenter and sample A_c is then used to calculate the hardness of the sample:

$$H = \frac{P_{max}}{A_c} \tag{2.10}$$

With nanoindentation the length scale of the indentation depth lies within nanometers in contrast to microns and millimeters in conventional hardness testing. This leads to the application of nanoindentation to extract mechanical properties of small-scale specimens, such as thin films or single grains, or surface treated samples. While hardness is the most straightforward property to gain out of nanoindentation experiments, they can also be used to calculate elastic modulus, strain-hardening exponent, fracture toughness and viscoelastic properties. The most common indenter geometry used for nanoindentation is a Berkovich indenter, which is represented by a three-sided pyramid with a face angle of 65.27° [55].

2.6.1 Oliver-Pharr method

The main difference between conventional hardness testing and instrumented indentation testing, besides the penetration depth, is the determination of the contact area between indenter and sample. While in conventional testing the contact area is calculated from direct measurements of the residual impression of the indent, this is not possible with nanoindentation, as the indents are too small to be measured accurately. Instead, the displacement of the indenter into the material is recorded throughout the experiment and together with the known indenter geometry the contact area can be calculated using the method by Oliver and Pharr [56]. Figure 2.17 (a) shows a typical load-displacement curve recorded during an indentation experiment. The indenter is pushed into the material surface until it reaches a certain maximum load P_{max} and maximum depth h_{max}, causing elastic-plastic deformation under the tip. During unloading of the indenter, the elastic displacement recovers and the final indentation depth h_f remains. Figure 2.17 (b) depicts a schematic cross-section of an indent during and after the indentation.

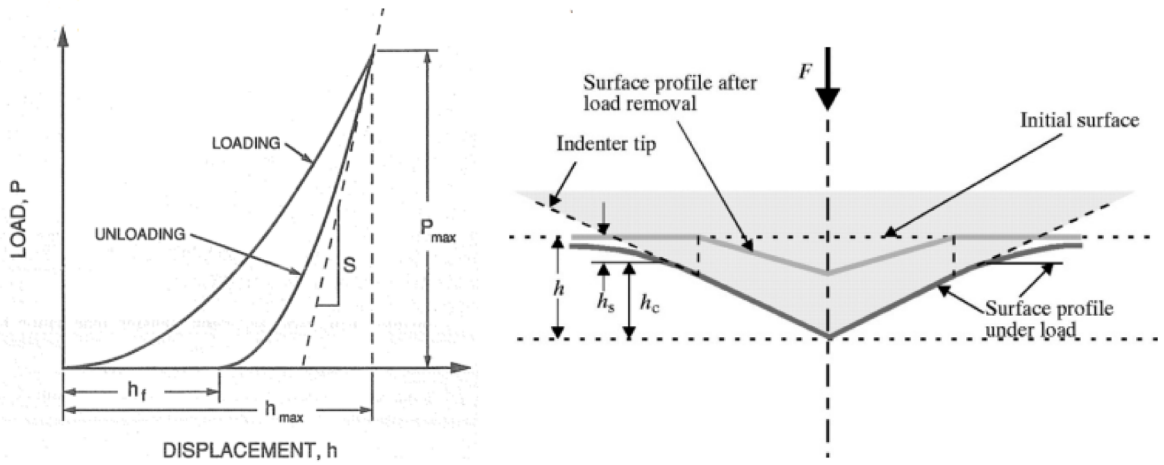

(a) **(b)**

Figure 2.17 (a) Load-displacement data of an indentation experiment. (b) Schematic of a section through an indent with parameters used for the analysis [56].

The evaluation of hardness and Young's modulus from indentation experiments as proposed by Oliver and Pharr [56] is described in the following.
In order to determine the contact area A_c for Equation 2.10, it is essential to calculate the contact depth h_c:

$$h_c = h_{max} - h_s \tag{2.11}$$

where h_{max} represents the maximum displacement and h_s the displacement of the surface at the perimeter of the contact (Figure 2.17 (b)). The maximum depth can be directly obtained from the load-displacement curve, while h_s depends on the indenter geometry and can be determined using Sneddon's elastic contact theory [57]:

$$h_s = \varepsilon \frac{P_{max}}{S} \tag{2.12}$$

where ε is a geometric constant (for a Berkovich indenter ε = 0.75) and S is the contact stiffness. The contact stiffness is also obtained from the load-displacement data, as it is the slope of the tangent of the unloading curve at the peak load P_{max} (see Figure 2.17 (a)). Usually the determination of S is carried out computer aided, as slight variations of the tangent can lead to significant differences in contact stiffness values.

Combining Equations 2.11 and 2.12 leads to:

$$h_c = h_{max} - \varepsilon \frac{P_{max}}{S} \tag{2.13}$$

Equation 2.13 allows the contact depth to be determined using only parameters that can be obtained from the load-displacement curve and a predefined geometry factor. Once h_c is calculated, the contact area A_c is determined by the area function:

$$A_c(h_c) = C_o\, h_c^2 + C_1\, h_c + C_2\, h_c^{1/2} + C_3\, h_c^{1/4} + C_4\, h_c^{1/8} + ... \tag{2.14}$$

with C_o describing an ideal indenter geometry (C_o = 24.5 for a Berkovich indenter) and the other constants C_i describing the deviations from an ideal tip. For each tip these constants have to be re-obtained from time to time by calibrations to take into account the inevitable blunting of the tip after several indents.
Finally, the contact area can be used to calculate the hardness using Equation 2.10.

The reduced modulus E_r is derived using:

$$E_r = \frac{\sqrt{\pi}}{2\beta} \frac{S}{\sqrt{A_c}} \tag{2.15}$$

where β represents a geometrical constant (for a Berkovich indenter β = 1.034). The reduced modulus combines the elastic properties of the indenter tip and the tested material through the relation:

$$\frac{1}{E_r} = \frac{1-\nu^2}{E} + \frac{1-\nu_i^2}{E_i} \tag{2.16}$$

with E and ν being the Young's modulus and Poisson's ratio of the specimen and E_i and ν_i of the indenter tip, respectively. For diamond, the most common indenter material, E_i = 1141 GPa and ν_i = 0.07.

2.6.2 Continuous stiffness measurement

Several dynamic nanoindentation techniques have recently been developed where an oscillating load with amplitude P_o and frequency ω is applied:

$$P = P_o\, e^{i\omega t} \tag{2.17}$$

The respective displacement response has the same frequency but might have a phase shift ϕ:

$$h = h_o\, e^{i(\omega t + \phi)} \tag{2.18}$$

The contact stiffness S can be calculated using P_o, h_o, ϕ and several system parameters, such as indenter mass, dampening coefficients and spring constants. Once S is obtained, the contact area and, as a consequence, hardness and modulus can be calculated using the equations stated in the previous section [55].
A popular method using this approach is continuous stiffness measurement (CSM). With CSM a conventional indenter loading curve is super-imposed with a small oscillating signal (see Figure 2.18). This way, the contact stiffness is measured continuously as the penetration depth of the indenter increases. This allows the determination of hardness and Young's modulus as a function of indentation depth and is therefore a popular tool used for indentation size effect (ISE) studies. CSM is also suitable for obtaining creep and fatigue properties [58, 59].

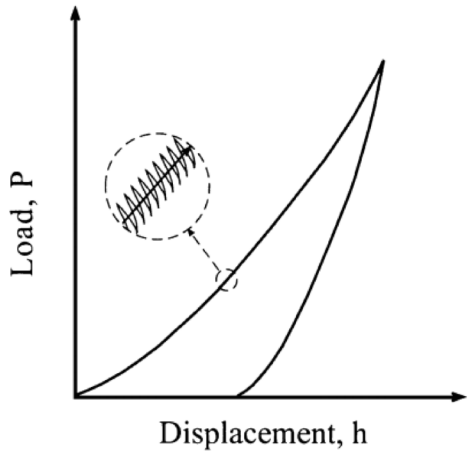

Figure 2.18 Schematic of the CSM displacement response [58].

2.6.3 Nanoindentation of irradiated materials

As outlined in Section 2.5, nanoindentation is a powerful tool to study mechanical properties of ion-irradiated materials. However, some difficulties arise with interpreting the obtained results, originating in the nature of both the irradiation treatment as well as the testing method. As is depicted in Figure 2.19, the plastic zone generated by indentation is much larger than the indent itself. Given the limited penetration depth and inhomogeneous dose profile of ion irradiation, this leads to a wide range of dose being sampled even with shallow indents. Additionally, shallow indents underlie the ISE, meaning they show higher hardness than the bulk hardness value. This is due to the large strain gradients imposed by the indent, leading to the formation of geometrically necessary dislocations and, hence, increased hardening [60]. These overlying phenomena yield a complicated situation in terms of analyzing and interpreting the indentation results. One way to mitigate these problems is to perform cross-sectional indents, as is shown in Figure 2.19 (b). These indents yield a good correlation of hardness and dose and make it easy to compare mechanical properties of irradiated and unirradiated areas. However, higher beam energies as well as time-consuming sample preparation after the irradiation is necessary using this approach. While preparing the sample surface for cross-sectional indents via mechanical polishing might influence the mechanical properties of said surface, electrochemical polishing results in rounded edges, making indent placement in these areas impossible. Therefore one has to consider which sample preparation process is suitable and yields the least restrictions for subsequent indentation.
As a rule, all indents on irradiated materials should be performed in a displacement controlled fashion to ensure they probe the same volume and thus dose range [53,54].

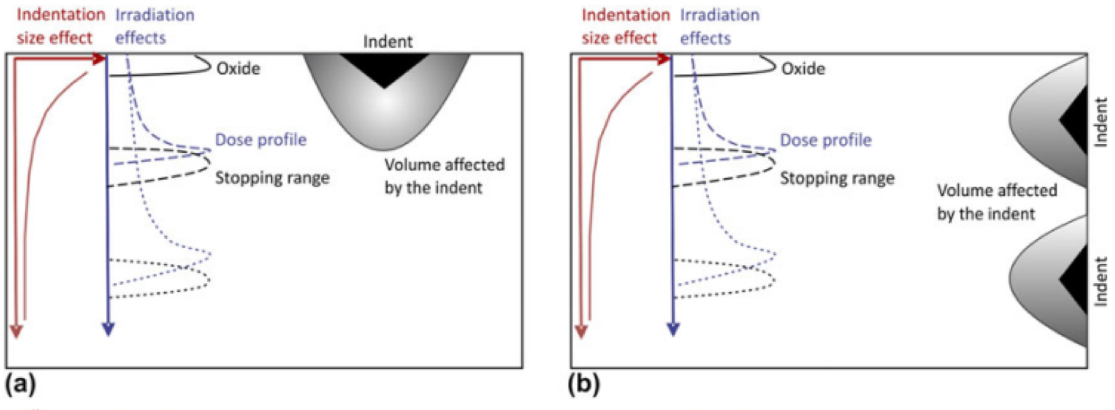

Figure 2.19 Schematic of irradiated material testing. Indentation performed (a) parallel and (b) perpendicular to the ion beam [53].

3 Experimental Methodology

This chapter will give an overview of the experimental procedure of this work, including details on fabrication, irradiation, microstructural investigation and mechanical testing of UFG, NC and NP composites.

3.1 Material fabrication

3.1.1 Powder consolidation

The fabrication route for all investigated materials starts out with the same basic steps. The raw materials, copper powder (99.9% purity, -625 mesh, 20 µm), iron powder (99+% purity, -200 mesh, 74 µm) and silver powder (99.9% purity, -500 mesh, 25 µm), were mixed together at a ratio of 50 at.% Cu, 25 at.% Fe and 25 at.% Ag ($Cu_{50}Fe_{25}Ag_{25}$) or 43.7 wt.%, 19.2 wt.% and 37.1 wt.%, respectively. The powder mixture was compacted using hot-isostatic pressing (HIP) at 630°C under a pressure of 30 MPa for 15 minutes. The HIP-process was conducted under vacuum to ensure as little impurities as possible. The powder consolidation resulted in small material cylinders with a radius of 4 mm and a height of 15 mm. The microstructure of the HIP-compacted samples was investigated using a light microscope (LM; Olympus BX51, Olympus Coorporation, Tokyo, Japan) and a scanning electron microscope (SEM; LEO type 1525, Carl Zeiss GmbH, Oberkochen, Germany).

3.1.2 High Pressure Torsion

In order to get a suitable sample geometry for the HPT process, the cylinders were cut into 1 mm thick disks using a precision saw (Secotom-10, Struers GmbH, Willich, Germany). The disks were deformed for 100 revolutions with a rotation speed of 0.6 turns per minute under a constant pressure of 5 GPa using a small HPT tool at

the Department of Materials Physics in Leoben. An air cooling system was used to counteract sample heating by friction and uphold a constant temperature throughout the process. The imposed maximum shear strain can be estimated using Equation 2.6 and yields $\gamma = 2513$. After the HPT deformation, the sample thickness was reduced to approximately 0.2 mm. For further processing, the HPT-deformed disks were cut into eight equally sized pieces with a diamond wire saw (Model 3242, Well Diamond Wire Saws Inc., Le Locle, Switzerland) as depicted in Figure 3.1. The resulting microstructure of the disks was investigated using the SEM.

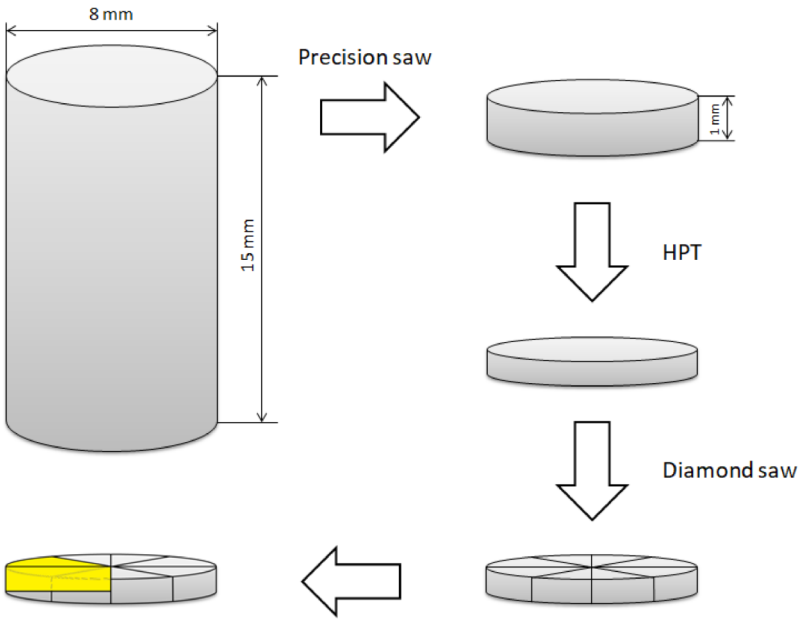

Figure 3.1 Schematic of the sample preparation process. The HIP-compacted cylinders are cut into 1 mm thick disks. After the HPT deformation, the disks are cut into eight equally sized pieces. The last sketch highlights the shape of a sample that is now ready for heat treatment and subsequent processing steps.

3.1.3 Heat treatment

To accomplish a reduction of the forced mixing of the components, heat treatments were performed using a muffle furnace (Heraeus GmbH, Hanau, Germany). In order to obtain materials with varying interface spacing and grain size, samples were annealed either at 400°C or 600°C for 1 hour. This yielded sample batches with finer grain size (henceforth referred to as NC samples) and coarser grain size (UFG samples) that were characterized using the SEM and the TEM. Differential scanning calorimetry (DSC; DSC 3+, Mettler Toledo Inc., Columbus, USA) was performed on a sample prior to the heat treatments to identify the exothermic peak that indicates

phase separation. The DSC was conducted in a nitrogen atmosphere with a heating rate of 20 K/min.

3.1.4 Foam processing

To obtain the various electrochemical potentials, open-circuit potential (OCP) measurements of pure Fe, pure Cu and $Cu_{50}Fe_{25}Ag_{25}$ were conducted in an electrochemical cell. All samples were polished prior to the mesasurements to ensure a uniform corrosion rate. Platin served as counter electrode, the reference electrode was a saturated calomel electrode (SCE) and 2 molaric (5 wt.%) HCl was used as electrolyte. A potentiostat (Gamry PCI4, Gamry Instruments Inc., Warminster, USA) recorded the measurement and the software Gamry Framework (Version 6.04) was used for analyzing the data.

The same electrochemical cell and experimental setup was used for foam processing. The protective potential for the potentiostatic dealloying was chosen as -450 mV, following the OCP results (as discussed in Section 4.2.1). Foam processing experiments were conducted at RT for various time spans with both the UFG and NC material as precursor. To take into account the plastic zone formed during nanoindentation as well as the penetration depth of the proton irradiation, a minimum dealloying depth of 20 µm was desired, allowing 2 µm deep indents to not be influenced by underlying bulk properties. In order to investigate the dealloying depth, samples were ion polished in cross-section using an argon ion milling system (E-3500 Ion Milling, Hitachi High Technologies Pte Ltd, Japan) or a dual beam FIB-SEM (Quanta 3D FEG, FEI, Hillsboro, USA) and investigated using the SEM or FIB-SEM. The foam composition was characterized by energy dispersive X-ray spectroscopy (EDX; Software EDAX and AZtec).

3.2 Irradiation treatment

3.2.1 Proton irradiation

To study radiation effects on nanostructured materials, samples (NC, UFG and NP) were irradiated with 1 MeV protons at the Ion Beam Materials Laboratory (IBML) at Los Alamos National Laboratory (LANL) in New Mexico, USA. The computer software "Stopping Range of Ions in Matter" (SRIM) [61] was used to simulate the

irradiation and yielded a penetration depth of approximately 8 µm in the bulk samples and 10 µm in a NP sample (assuming total dissolution of Fe).
The dose D in dpa can be calculated using the following formula:

$$D = \frac{N_V \cdot N_I}{\rho_N} \tag{3.1}$$

with N_V as the number of vacancies produced per ion and angstrom, N_I the number of ions (protons) contributing to the damage and ρ_N the number density of the irradiated material in atoms per angstrom. While N_V can be calculated by SRIM simulations, the number of protons is determined via:

$$N_I = \frac{I}{q} \cdot t \tag{3.2}$$

where I is the beam current in C/s, q the charge of the ion ($q = 1.602 \cdot 10^{-19}$ C for protons) and t the length of the ion-beam irradiation in s. The number density is calculated using:

$$\rho_N = \rho_A \cdot A \tag{3.3}$$

with ρ_A as the atomic density ($\rho_A = 7.815 \cdot 10^{22}$ and $7.343 \cdot 10^{22}$ atoms per cm^3 for the bulk and NP material, respectively) and A the irradiated surface area.

The value for N_V in the plateau before the stopping peak was obtained by SRIM calculations and estimated to be $7.2 \cdot 10^{-5}$ vacancies per ion and angstrom. The proton-beam current was 3 µA in average and the beam spot size was 4 x 6 mm. Using the equations above an approximate irradiation time of 38.6 hours was estimated to reach 1 dpa plateau dose in the bulk material. An x-ray emission detector was used to obtain the exact number of protons that hit the target.

3.2.2 Helium implantation

For the investigation of helium-induced swelling and property changes, bulk samples were implanted with helium using a helium-ion microscope (Orion NanoFab, Carl Zeiss GmbH, Oberkochen, Germany). The irradiation was conducted with 25 keV

He-ions, which corresponds to a penetration depth of about 200 nm according to SRIM. NC and UFG samples were irradiated to doses of $1 \cdot 10^{17}$, $3 \cdot 10^{17}$, $4 \cdot 10^{17}$, $5 \cdot 10^{17}$, $7.5 \cdot 10^{17}$ and $1 \cdot 10^{18}$ ions/cm^2, respectively. The helium was implanted in 10 x 10 µm^2 squares on the surface.

3.3 Atomic force microscopy

The helium-induced swelling of the bulk material was measured using an atomic force microscope (AFM; Nanoscope III-A, Digital Instruments, Santa Barbara, USA) at the Department of Nuclear Engineering in Berkeley, CA, USA. The mode of operation for this AFM is depicted in Figure 3.2. The sample is mounted on a tube that consists of several piezo elements, which allows it to be moved in x-, y- and z-direction when a respective voltage is applied. Laser light (λ = 632 nm) is sent through a prism to the back of a cantilever that is scanning the sample surface. Depending on the atomic force repulsion or attraction of the sample surface, the cantilever changes its altitude and thus also the direction of the reflected laser light. This deflection is measured with a photodiode detector and the respective data is recorded. This allows a precise reconstruction of the sample surface topology. A feedback loop regulates the movement of the piezo tube stage.

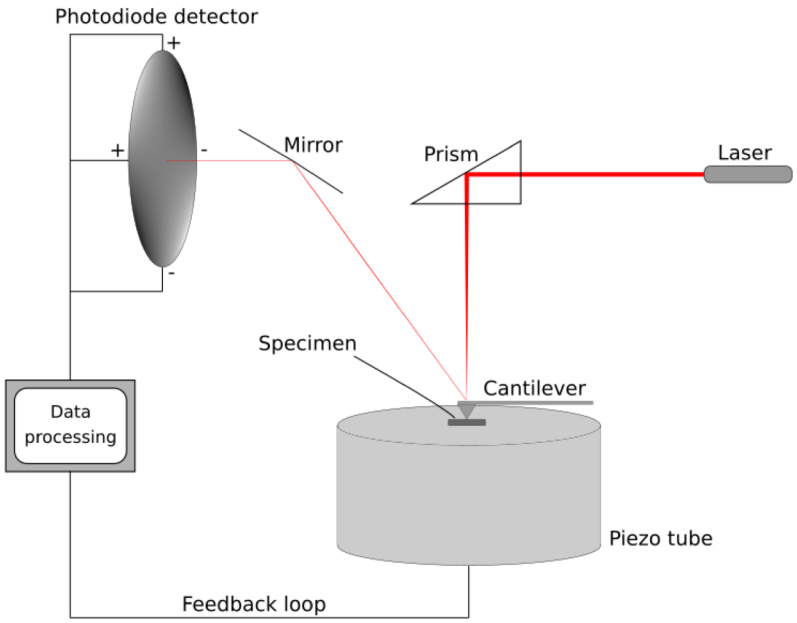

Figure 3.2 Working principle of the Nanoscope III-A AFM.

The helium-implanted areas on UFG and NC samples were investigated in tapping mode. The analysis was carried out using the software NanoScope III, Gwyddion and Origin.

3.4 Nanoindentation

Pre- and post-irradiation indents were performed using a nanoindenter (Micro Materials NanoTest Platform 3, Micro Materials Inc., Wrexham, UK) at the Department of Nuclear Engineering in Berkeley. Figure 3.3 shows the configuration and working principle of the indenter. The indenter tip is mounted on a movable pendulum that can be controlled by a magnetic field produced by a coil. Depending on the applied voltage, the pendulum applies a certain load on the indenter tip, pushing it into the sample surface. The indenter is equipped with an optical microscope with four different magnifications, allowing precise placement of indents on the specimen.

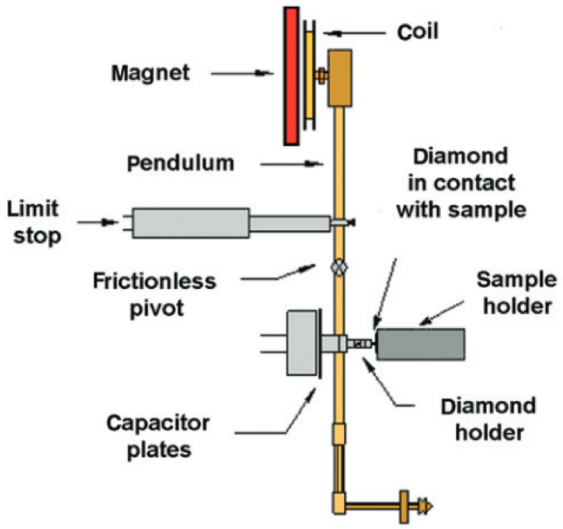

Figure 3.3 Schematic sketch of the Micro Materials nanoindenter [62].

All indentations were conducted at RT using a diamond Berkovich tip. For each tip the sample stage and crosshair calibrations were performed and an area function was obtained using fused silica. Bulk samples were polished prior to the indentation to reduce possible effects of surface roughness on the measurement. Indentations were performed in a displacement controlled fashion as outlined in Section 2.6.3. As well-polished bulk materials are expected to show stable values for hardness and modulus already at relatively small indentation depths, UFG and NC samples were indented to a depth of 500 and 1000 nm. NP samples, however, were indented to a

depth of 1000 and 2000 nm due to the high surface roughness and porosity, which would result in a large scatter of data for small indentation depths, depending if the indenter tip hits more foam ligaments or pores. The load was applied with a fixed rate of 5 mN/s, a dwell period of 15 s at the peak load and an unloading rate of 10 mN/s. A minimum of 10 indents per sample and indentation depth was performed. To take into account thermal drift, a thermal drift correction was conducted after each indentation, using the last 60% (36 s) of the recorded drift data. The thermal drift for all measurements did not exceed 0.3 nm/s. The data was recorded and evaluated using the software NanoTest Platform Three and Origin.

3.4.1 Continuous stiffness measurement

To investigate the mechanical properties of the helium-implanted samples, CSM-indentations were conducted using a TI 950 Triboindenter (Hysitron Inc., Eden Prairie, USA) with an in-situ scanning probe microscopy (SPM) and nanoDMA (nanoscale Dynamic Mechanical Analysis) option at the Department of Materials Science and Engineering in Berkeley. This indenter uses a three-plate capacitive transducer for both applying the load and measuring the indentation depth.
After the calibrations were performed, the regions of interest on the specimens were mapped using the SPM option, allowing indents to be placed within 10 nm of accuracy. Indentation experiments were conducted on implanted and unimplanted areas, following the load function depicted in Figure 3.4. After contact with the sample has been made, the indenter is withdrawn for 2 seconds (red part). Subsequently, a quasi-static load is applied for 3.5 seconds, followed by an exponential dynamic nanoDMA-loading (green part). After a dwell time of 2 seconds at peak load, the unloading is carried out linearly. A peak load of 6000 µN for the softer UFG material and 9000 µN for the harder NC samples was chosen in order to get similar indentation depths of about 250 nm. For each helium dose, 5 indents were performed in the implanted area and several control indents in unimplanted regions. The analysis of the indentation results was performed using the software TriboScan and Origin.

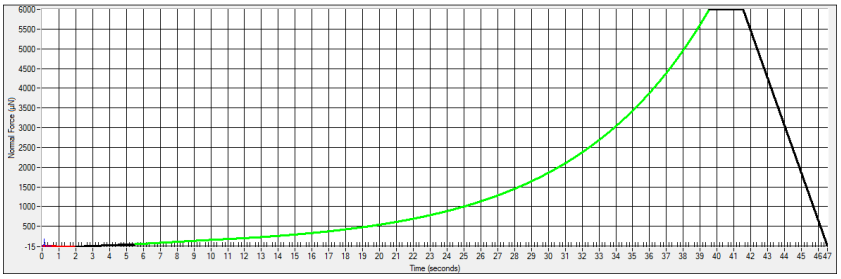

Figure 3.4 The load function used for the CSM indents.

To get a better resolution of mechanical property changes with dose, additional CSM-indentation measurements were performed on the proton-irradiated material with a Keysight Nano Indenter G200 (Keysight Technologies Inc., Santa Rosa, USA) at the Department of Materials Physics in Leoben. Indents were performed parallel to the ion-beam to a displacement of 2500 nm as well as cross-sectional to a displacement of 1000 nm (compare with Figure 2.19).

4 Results

4.1 Material processing

The powder consolidation via HIP resulted in a three-phased composite (Figure 4.1). The three components can be distinguished by their phase contrast, i.e. ability to scatter electrons. Iron, as the lightest element, scatters less electrons and appears therefore darker than the heavier copper. Silver, however, is the heaviest element in the alloy and therefore also the brightest in SEM images. The coarse phase sizes of the different components (in the tens of microns) can be explained by the initial powder grain sizes. Although the HIP-process was conducted under vacuum, oxides were observed in the compacted samples, in particular for iron grains.

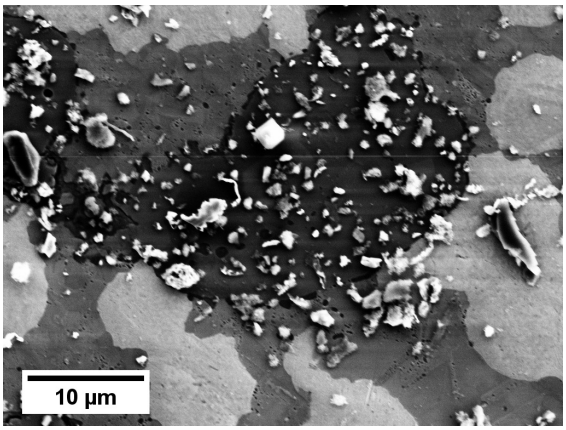

Figure 4.1 SEM image (back scattered electron mode) of the microstructure of the HIP-compacted material.

Figure 4.2 shows the resulting microstructure after the HPT deformation. Three-phased lamellas and shear bands are visible in a 0.5 mm wide region around the center of the HPT disks. The rest of the material shows a uniform, single-phased microstructure with a few oxides and pores. This indicates that here the deformation was high enough to introduce a sufficient amount of defects into the material in order to enhance diffusion and thus mechanically alloy the three immiscible components into one phase.

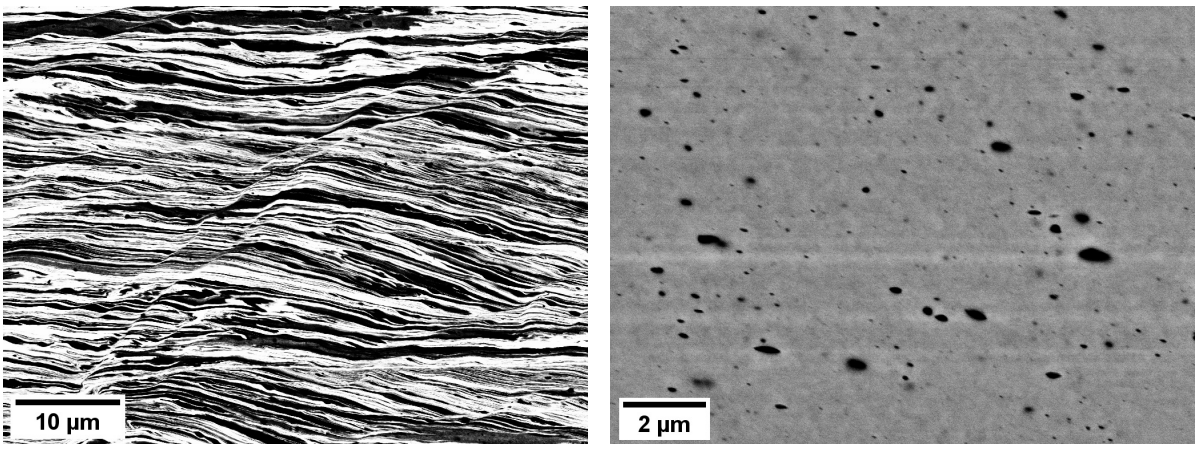

Figure 4.2 SEM images (back scattered electron mode) showing the microstructure after HPT deformation at (a) the center of the disk and (b) 3 mm from the center.

The DSC measurement results for the mechanically alloyed HPT samples are depicted in Figure 4.3. The exothermic heat flow indicates an ordering process, i.e. phase separation, inside the material. The peak of the curve is at 287°C. At about 600°C the heat flow is reduced to its initial value again, indicating that the phases have completely separated and there is no more forced mixing in the material.

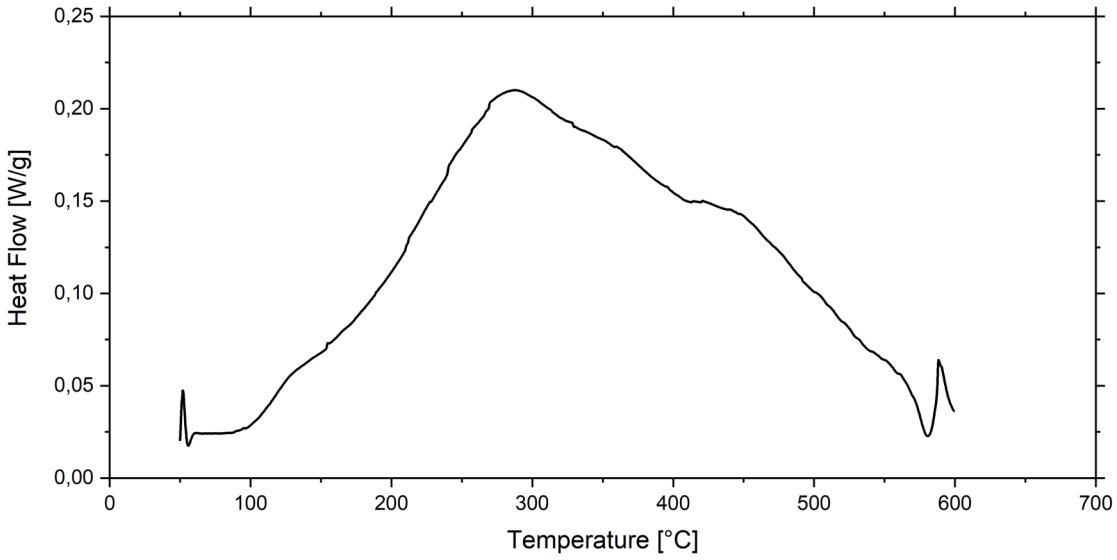

Figure 4.3 Obtained DSC curve for the mechanically alloyed, metastable material.

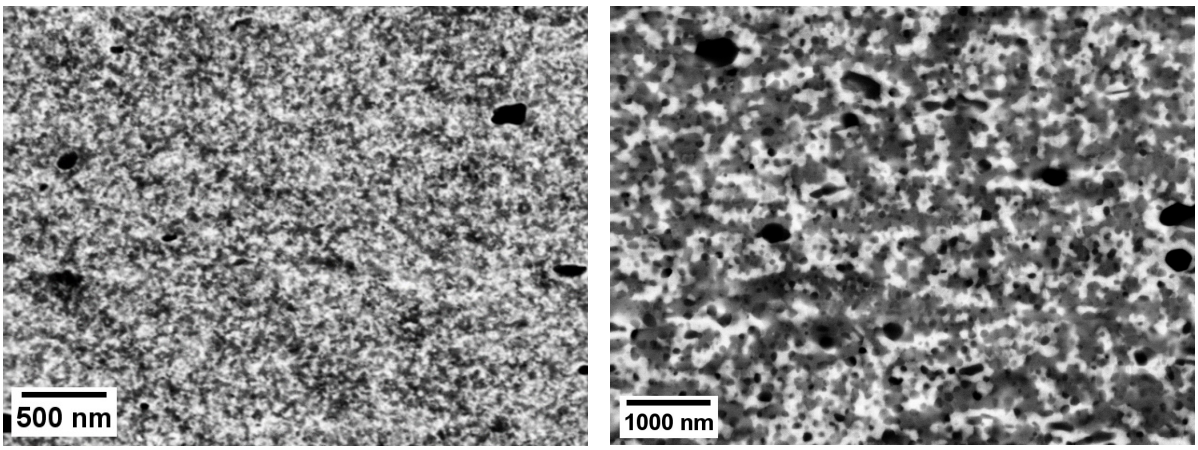

(a) **(b)**

Figure 4.4 SEM images (back scattered electron mode) showing the microstructure after annealing at (a) 400°C and (b) 600°C for 1 hour.

The microstructures after heat treatments at 400°C and 600°C for 1 hour are shown in Figures 4.4 and 4.5. The metastable single-phase successfully separated into its three original components again. Annealing at 400°C yielded a microstructure with an average phase size of about 18.8 ($\pm$ 1.8) nm, in contrast to a phase size of about 95.7 ($\pm$ 10.3) nm after the heat treatment at 600°C. This can be explained by increased grain growth at higher temperatures. Therefore, the finer grained sample represents a nanocrystalline material (<100 nm), whereas the other sample falls in the ultra-fine grained regime (100-500 nm).

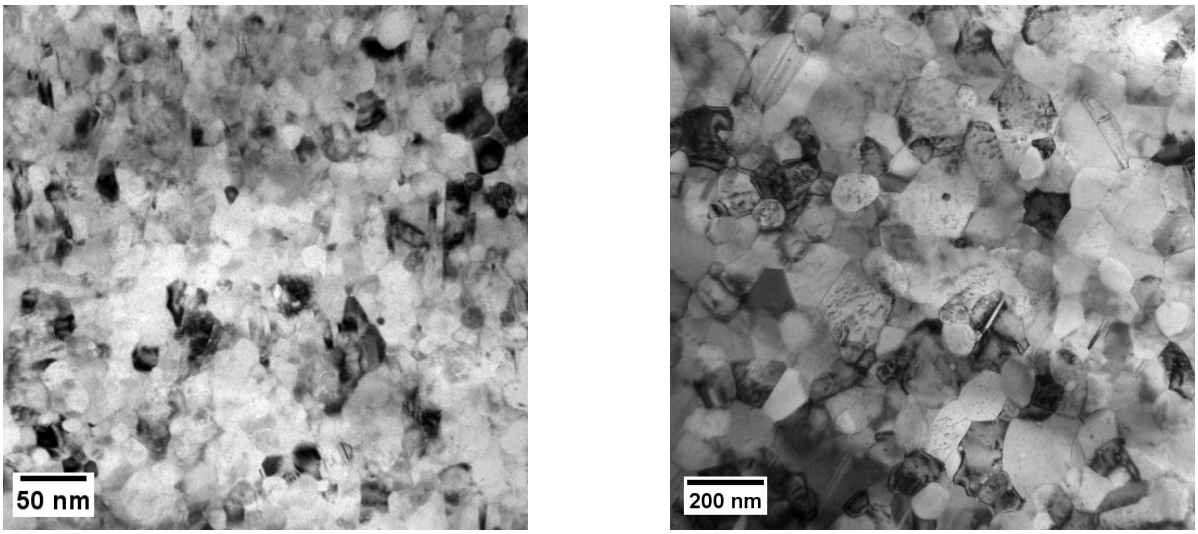

(a) **(b)**

Figure 4.5 TEM images showing the microstructure after annealing at (a) 400°C and (b) 600°C for 1 hour.

The composition of samples after the heat treatment was investigated via EDX analysis and is listed in Table 4.1. The values are in good agreement with the initial powder mixture.

Table 4.1 EDX results for representative samples of different material states.

Element	**initial**		**annealed**		**UFG foam 4h**		**NC foam 8h**	
	at.%	wt.%	at.%	wt.%	at.%	wt.%	at.%	wt.%
Cu	50.00	43.70	48.46	42.03	47.00	37.67	49.39	42.80
Fe	25.00	19.20	25.24	19.24	14.88	10.48	24.16	18.40
Ag	25.00	37.09	26.30	38.73	38.12	51.85	26.45	38.90
Σ	100	100	100	100	100	100	100	100

4.2 Foam manufacturing

4.2.1 Electrochemical measurements

The OCP curves for pure Fe, pure Cu and the Cu-Fe-Ag alloy in 2 molaric HCl are depicted in Figure 4.6. The measurements for each sample were conducted until the values reached a certain stability, indicating a quasidynamic equilibrium. The electrochemical potential of Cu-Fe-Ag lies above the potentials for Fe and Cu. Therefore both of these components act as anode within the alloy and their dissolution observed in the free corrosion experiments is explained.

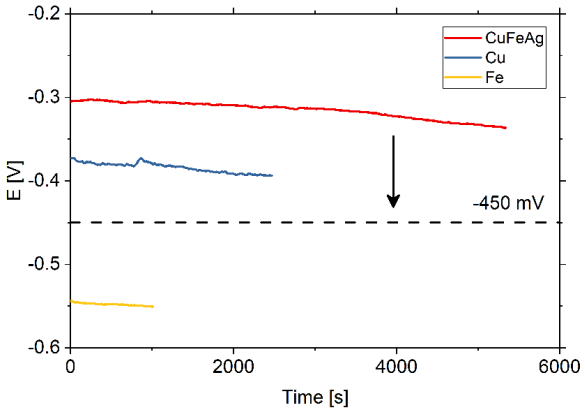

Figure 4.6 OCP measurement results and chosen potential for potentiostatic dealloying.

To overcome the dissolution of copper, a voltage has to be applied to push the potential of the Cu-Fe-Ag alloy beneath the OCP of Cu. A potential of -450 mV was chosen in order to ensure no dissolution of copper, while still providing enough driving force to dissolve iron in a reasonable amount of time.

4.2.2 Potentiostatic dealloying

The microstructure after potentiostatic dealloying of a UFG precursor for dissolution times of 4 and 24 hours are depicted in Figure 4.7 (a)-(d).

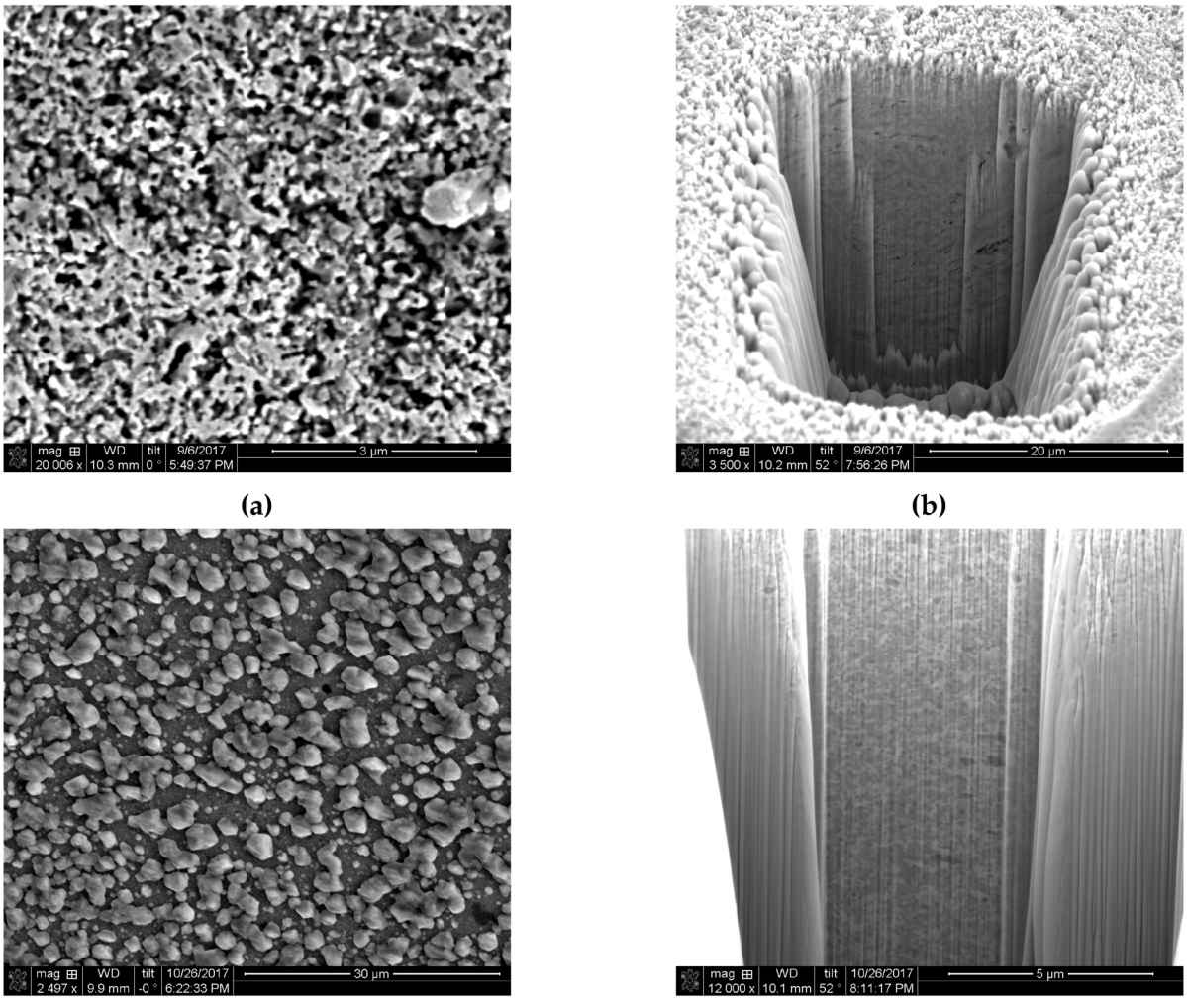

(a) **(b)**

(c) **(d)**

Figure 4.7 SEM images showing the microstructure after potentiostatic dealloying of a UFG sample for 4 hours: (a) surface and (b) subsurface microstructure. UFG sample for 24 hours: (c) surface and (d) subsurface microstructure.

While the foam after 4 hours dealloying shows good surface and decent subsurface porosity down to at least 20 µm, this was surprisingly not the case for the 24 hours sample. Several microns-big, roundish precipitations were covering the surface of this specimen. Additionally, no porosity was observed beneath the surface. EDX mapping revealed that the surface precipitations contain almost pure copper (Figure 4.8). Why this precipitations formed can not be explained at this point, but they might be the cause for the little porosity, as they could clog the way for the solution into the material or act as passivation layer.

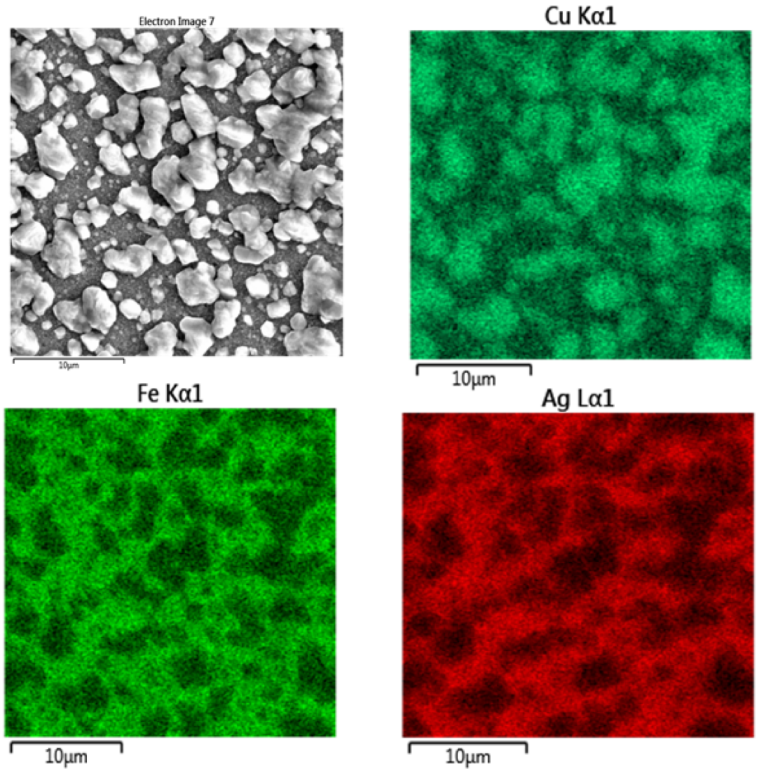

Figure 4.8 EDX mapping of the surface precipitations in UFG precursor after 24 hours dealloying.

The average composition of the foam that underwent the dealloying for 4 hours is also depicted in Table 4.1. These EDX results indicate that there is still iron in the foam and that there is still some copper dissolving, however by far not as much as in free corrosion experiments. This could be due to the fact that the sample still spends several minutes in the HCl solution before and after the voltage is applied, i.e. under free corrosion conditions. However, the goal of creating a multiphased, nanoporous material was achieved.

The microstructure after 8 hours dealloying of a NC precursor is apparent in Figure 4.9. Poor porosity is observed on the sample surface and practically no porosity

underneath. This can be explained by the small grain size of the sample, making it difficult for the solution to penetrate inside the material and for the dissolved components to get out. The heat treatment at 400°C might also yield an explanation. As is indicated by the DSC curve in Figure 4.3, there might still be considerable amount of forced mixing in the different grains after annealing at this temperature, making them resistant to the HCl solution.
EDX measurements of the composition showed almost no change from the initial composition of the precursor (Table 4.1).

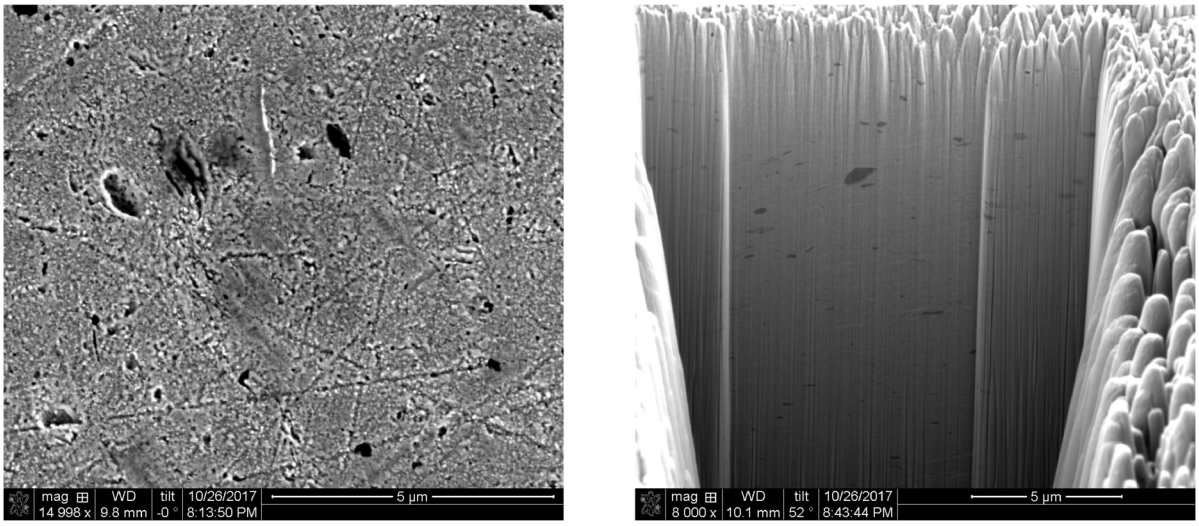

(a) **(b)**

Figure 4.9 SEM images showing the microstructure after potentiostatic dealloying of a NC sample for 8 hours: (a) surface and (b) subsurface microstructure.

As the 4 hours dealloyed UFG foam showed the most promising and reproducible results, it was chosen as NP sample for the radiation effect study in this work.

4.3 Proton irradiation effects

UFG, NC and NP samples were successfully irradiated with protons. The dose profile for the bulk (i.e. UFG and NC) as well as NP material was calculated using Equation 3.1 and is depicted in Figure 4.10.

To evaluate the effect of the irradiation on material properties, nanoindentation was performed. The results are displayed in the next section.

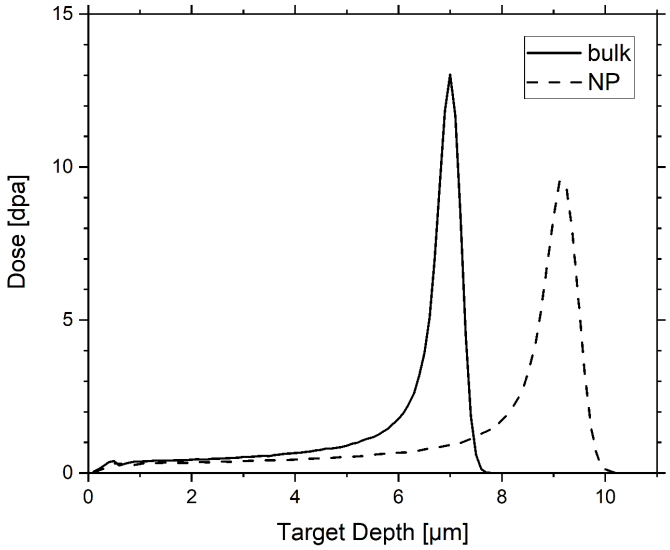

Figure 4.10 Dose profile for proton irradiation of bulk and NP material.

4.3.1 Bulk material

As the static nanoindentation on the proton-irradiated materials did not reveal a lot of information about dose-dependant hardness changes, additional CSM-indentation was performed at the Department of Material Physics in Leoben.

Perpendicular nanoindentation

Figure 4.11 shows the results of CSM-nanoindentation conducted directly onto the irradiated surface of UFG and NC material in comparison to the unirradiated material (black square).

All values lie within the range of the unirradiated material and show a more or less constant profile after an indentation depth of about 500 nm. For a non-radiation resistant material, one would expect to see the influence of the dose profile (especially of the stopping peak) in the hardness over depth curve. As this is not the case, it can be assumed that both materials do not show a notable hardening effect after proton irradiation. However, performing indentation on the irradiated surface yields a fairly complicated situation in terms of analyzing mechanical properties, as a lot of superposing effects (e.g. dose profile, ISE and other surface effects) can occur [53].

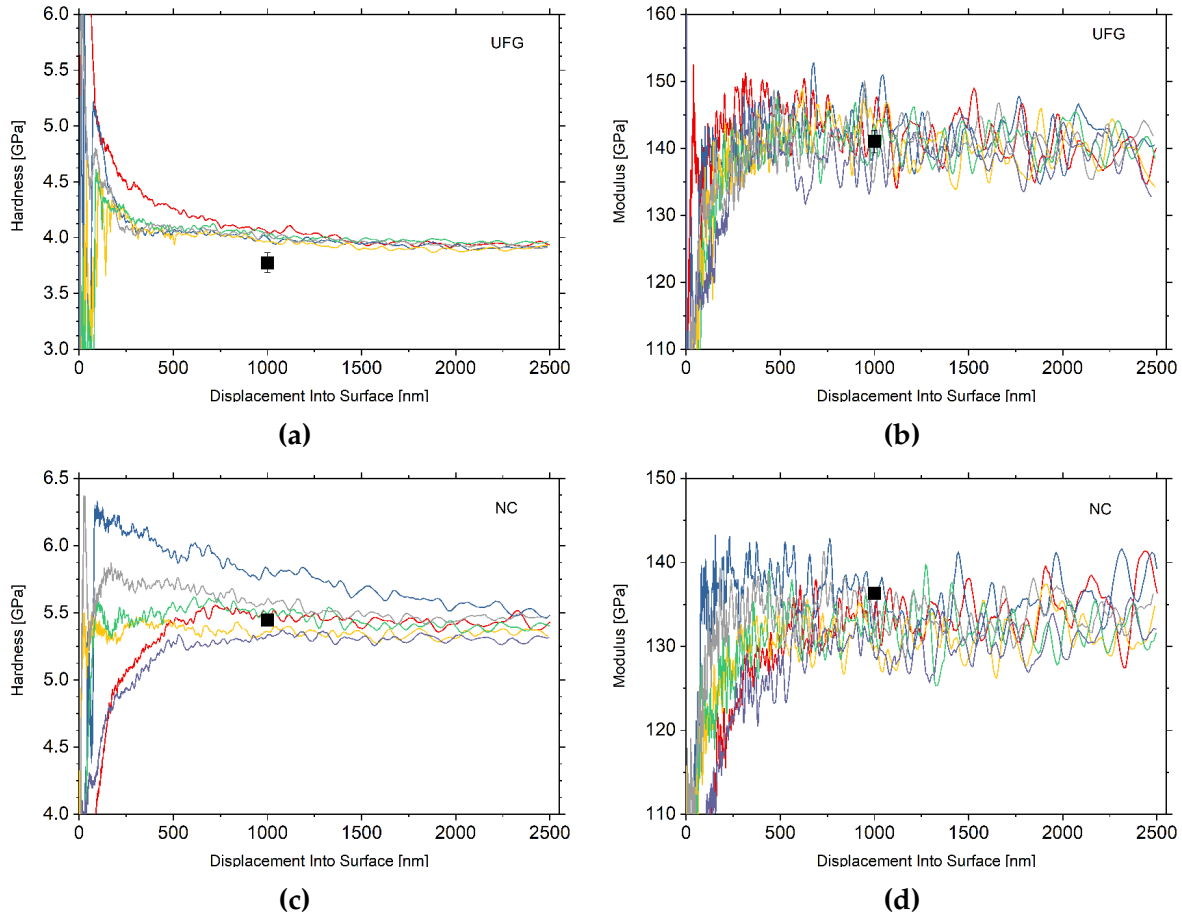

Figure 4.11 Results of perpendicular nanoindentation: (a) Hardness and (b) modulus of UFG material and (c) hardness and (d) modulus of NC material. The black square symbol represents the average unirradiated properties gained by indentation to 1000 nm depth.

In order to shed more light on the material response and confirm this material in its ability of tolerating radiation damage, additional cross-sectional indents were performed.

Cross-sectional nanoindentation

During investigation of the prepared cross-section with the LM before indentation, an odd phenomena caught the eye (see Figures 4.12 through 4.14). The edge of the irradiated layer was distinguishable by a slightly darker shaded line, about 7 µm from the surface. In the UFG material, additional pores were visible on this line. By comparing the distance of this line from the surface to the dose profile in Figure 4.10,

it is clear that the observed line represents the stopping peak of the proton irradiation. Figure 4.12 gives an overview on which indent represents which curve in the following graphs. The indents were placed with different distances from the surface and sample therefore different volume fractions of the irradiated layer. Additional indents were performed in the unirradiated bulk material for comparative reasons.

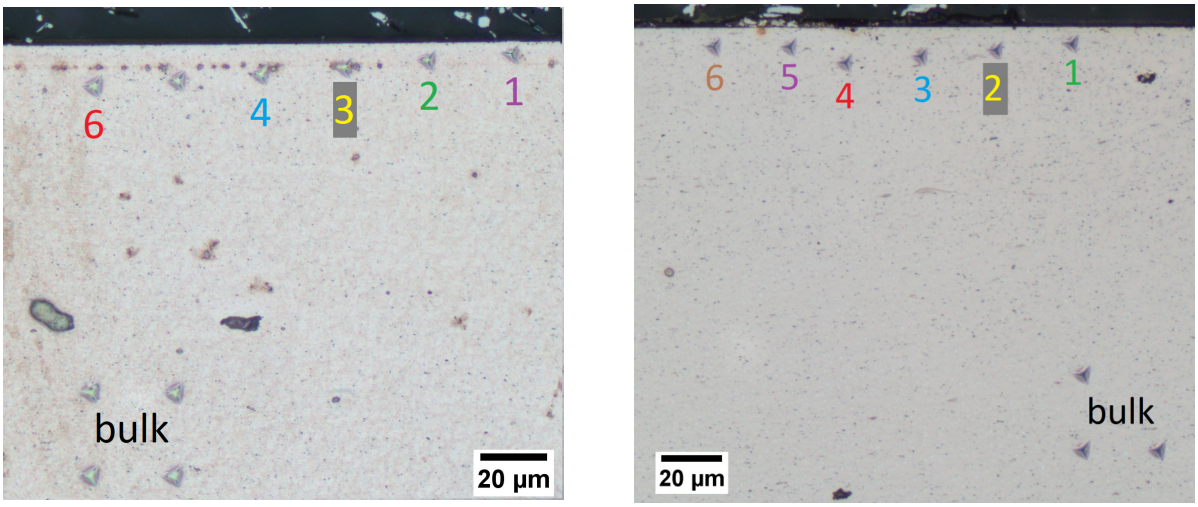

(a) (b)

Figure 4.12 Overview of cross-sectional indents in (a) UFG and (b) NC material.

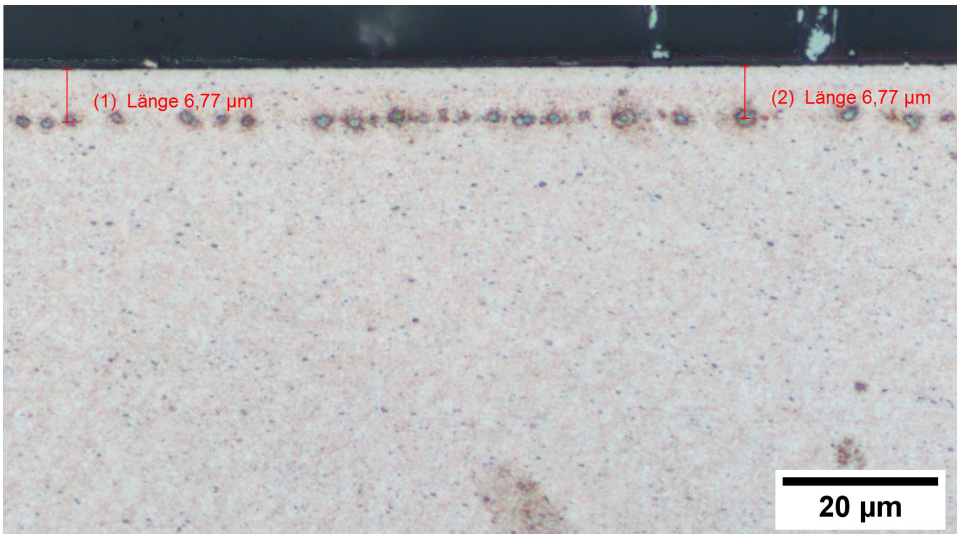

Figure 4.13 Detail of the observable stopping peak-line in UFG material.

Figure 4.15 shows the results of cross-sectional indents in UFG material. Both the hardness and modulus of indents in irradiated areas are lower then unirradiated properties, with the properties decreasing the closer the indent is to the surface.

Figure 4.14 Detail of the observable stopping peak-line in NC material.

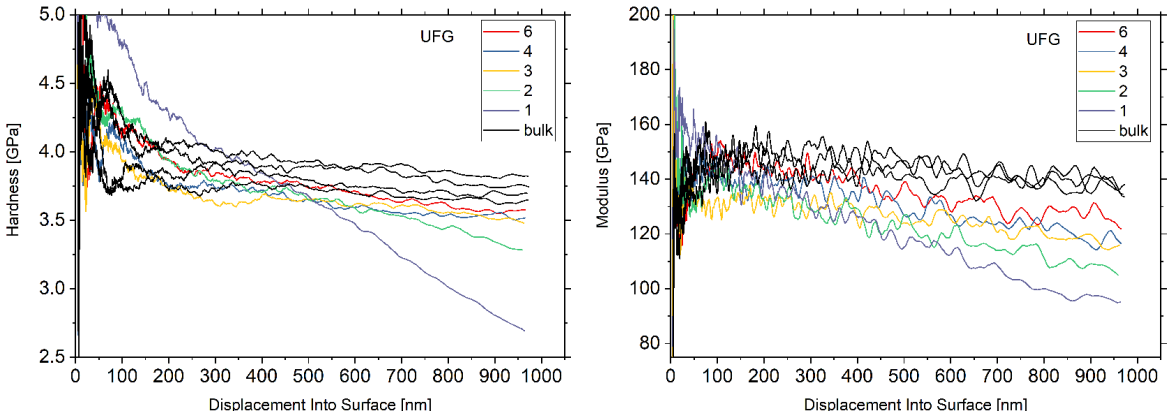

(a) **(b)**

Figure 4.15 Results from cross-sectional indentation of the proton-irradiated UFG material. The indent numbers represent the respective indents marked in Figure 4.12 (a). The black curves represent indents performed in the unirradiated bulk material.

A similar trend is observed in the NC material (see Figure 4.16) with the difference in hardness and modulus in irradiated and unirradiated areas being even bigger. To gather more information about radiation-induced property changes, additional indents were placed right on the stopping peak line (indents 2, 5 and 6 in Figure 4.12 (b)), where the indents are expected to probe the biggest volume fraction of irradiated material. These results are depicted in Figure 4.17.

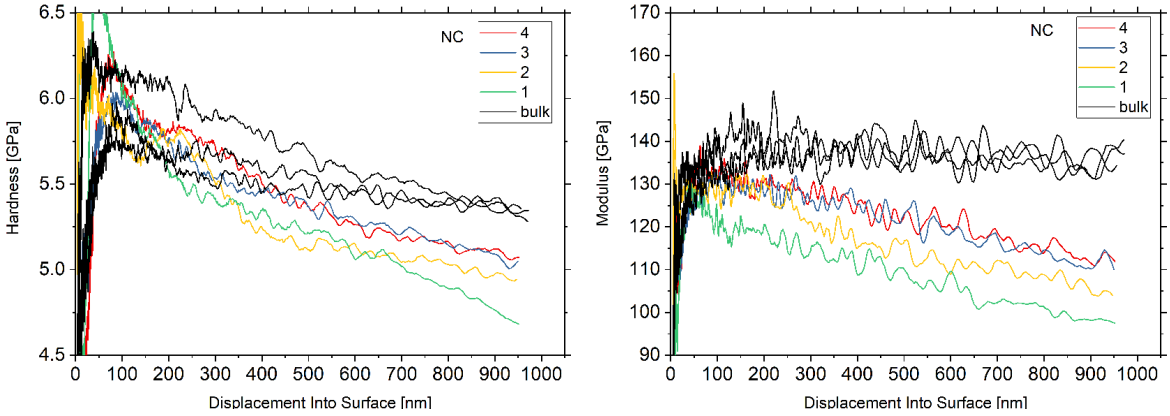

(a) **(b)**

Figure 4.16 Results from cross-sectional indentation of the proton-irradiated NC material. The indent numbers represent the respective indents marked in Figure 4.12 (b). The black curves represent indents performed in the unirradiated bulk material.

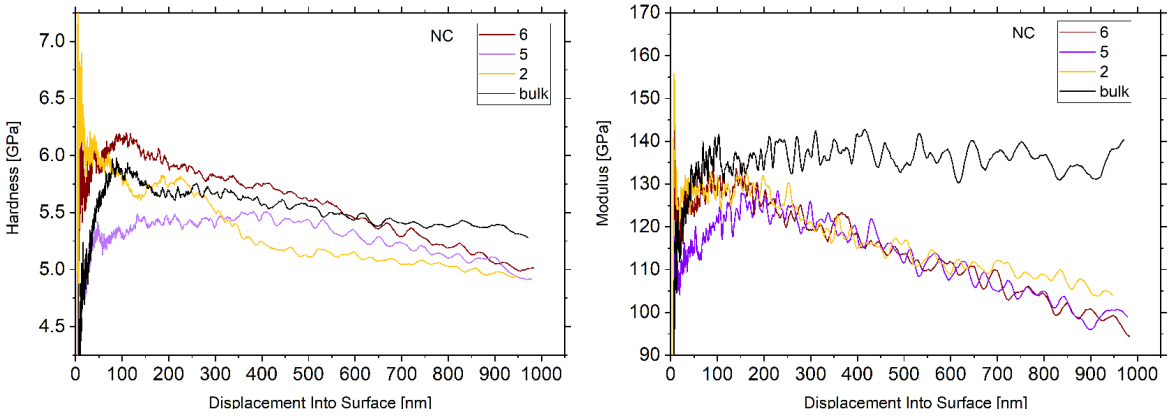

(a) **(b)**

Figure 4.17 Results from cross-sectional indentation on the stopping peak line in NC material. The indent numbers represent the respective indents marked in Figure 4.12 (b). The black curve represents an indent in the unirradiated bulk material.

4.3.2 Nanoporous material

Indentation of the NP material turned out to be rather difficult. Increased surface roughness and a very inhomogeneous porosity (and therefore also chemical composition) resulted in the measured mechanical properties being heavily dependant on the indent placement, as is apparent in Figure 4.18. Not a lot of information about the material response due to the irradiation can be gained from this data. However, an attempt was made in Section 5.2.2 by estimating the porosity under each indent.

As polishing NP samples would destroy the complicated foam-structure, performing cross-sectional indents on the NP material was not possible.

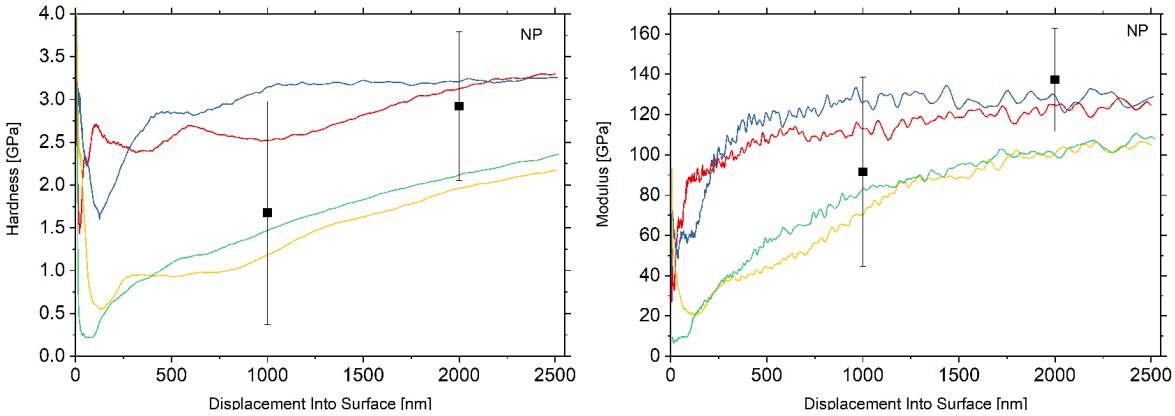

(a) **(b)**

Figure 4.18 Results from CSM-indentation of the proton-irradiated NP material. The black square symbols represent the average unirradiated properties gained by indentation to 1000 nm and 2000 nm depth.

4.4 Helium effects

UFG and NC samples were successfully implanted with different doses of helium-ions. The calculated dpa-profile for each dose is shown in Figure 4.19.

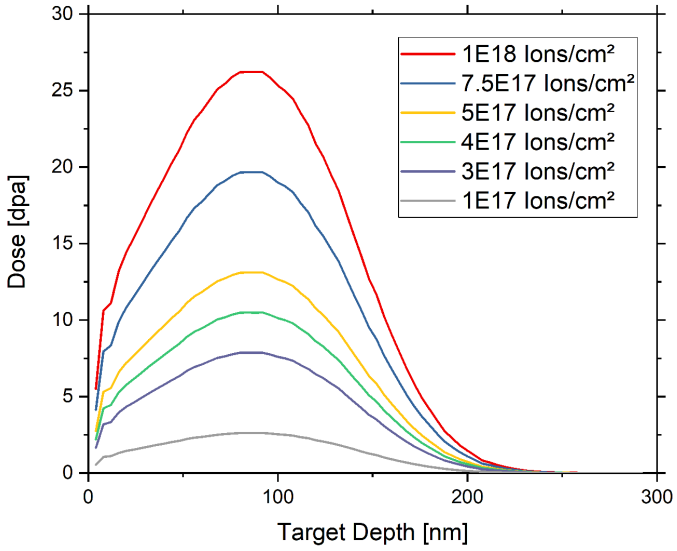

Figure 4.19 Dose profile for helium implantation with six different doses.

The helium-induced swelling of the samples was investigated per AFM, whereas the change of mechanical properties was characterized with shallow CSM-indentation. As both of these methods are highly sensitive to surface roughness, an evaluation of helium effects on the NP material was not possible.

4.4.1 Swelling

Figures 4.20 and 4.21 show the surface topology of helium-implanted regions in UFG and NC material gained by AFM measurements. Representative line plots of the implanted areas for each sample and dose were obtained from these AFM measurements. They are depicted in Figure 4.22. As the dose gets higher, so is the swelling height. For high doses of helium the UFG sample shows significantly more swelling and a higher surface roughness than the NC material. For lower doses the opposite can be observed, as the UFG sample showed less swelling after implantation with doses of 3 and 4 $\cdot 10^{17}$ ions/cm^2 than the NC specimen. The dose of $1 \cdot 10^{17}$ ions/cm^2 was not included in this plot, as it shows nearly no distinction

from unirradiated regions in both samples. This implies that there is no swelling or that the swelling lies within the range of the surface roughness.

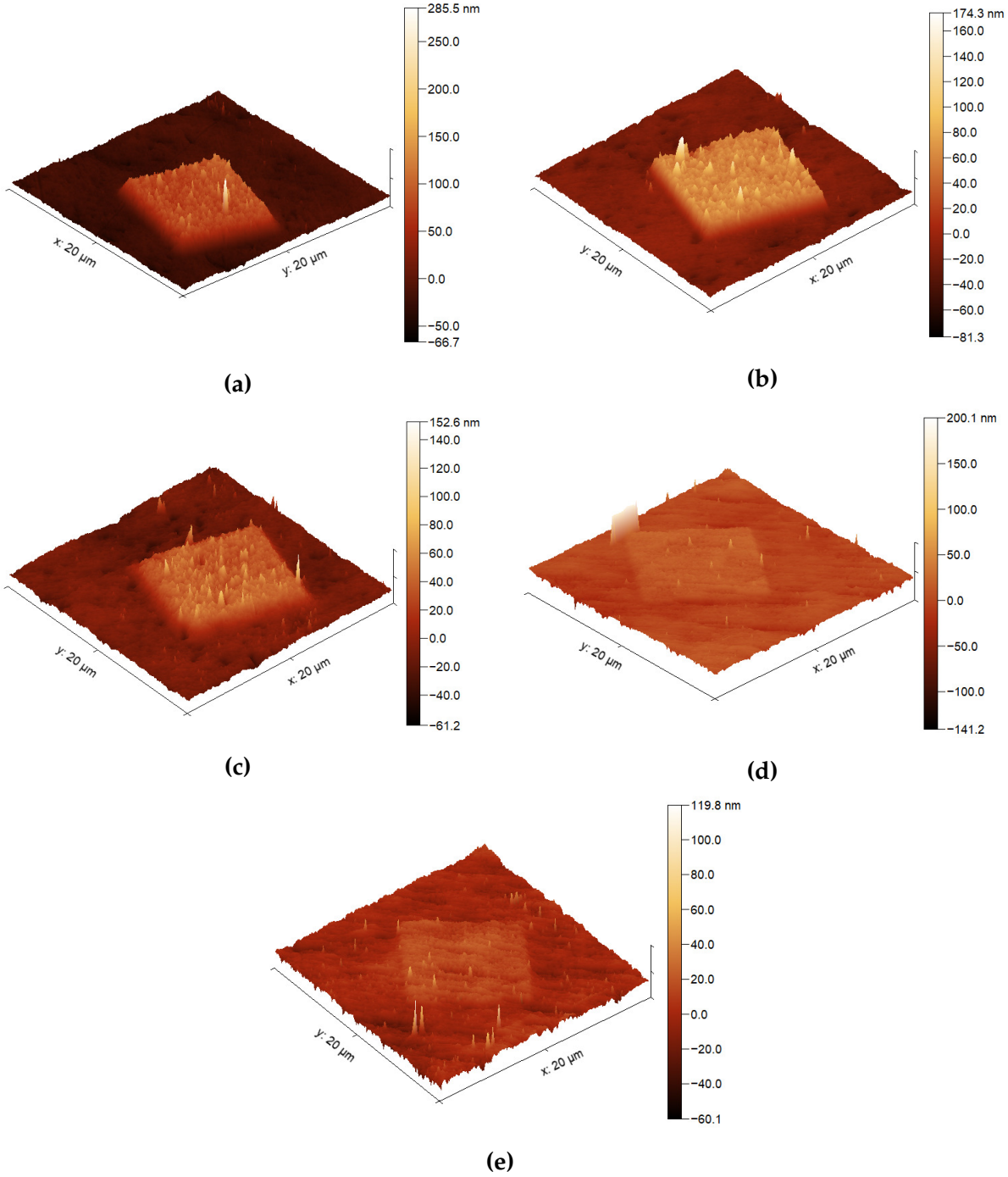

Figure 4.20 Three-dimensional reconstructions of the surface topology of helium implanted regions in UFG material gained by AFM measurements. Doses of (a) 1E18, (b) 7.5E17, (c) 5E17, (d) 4E17 and (e) 3E17 Ions/cm^2.

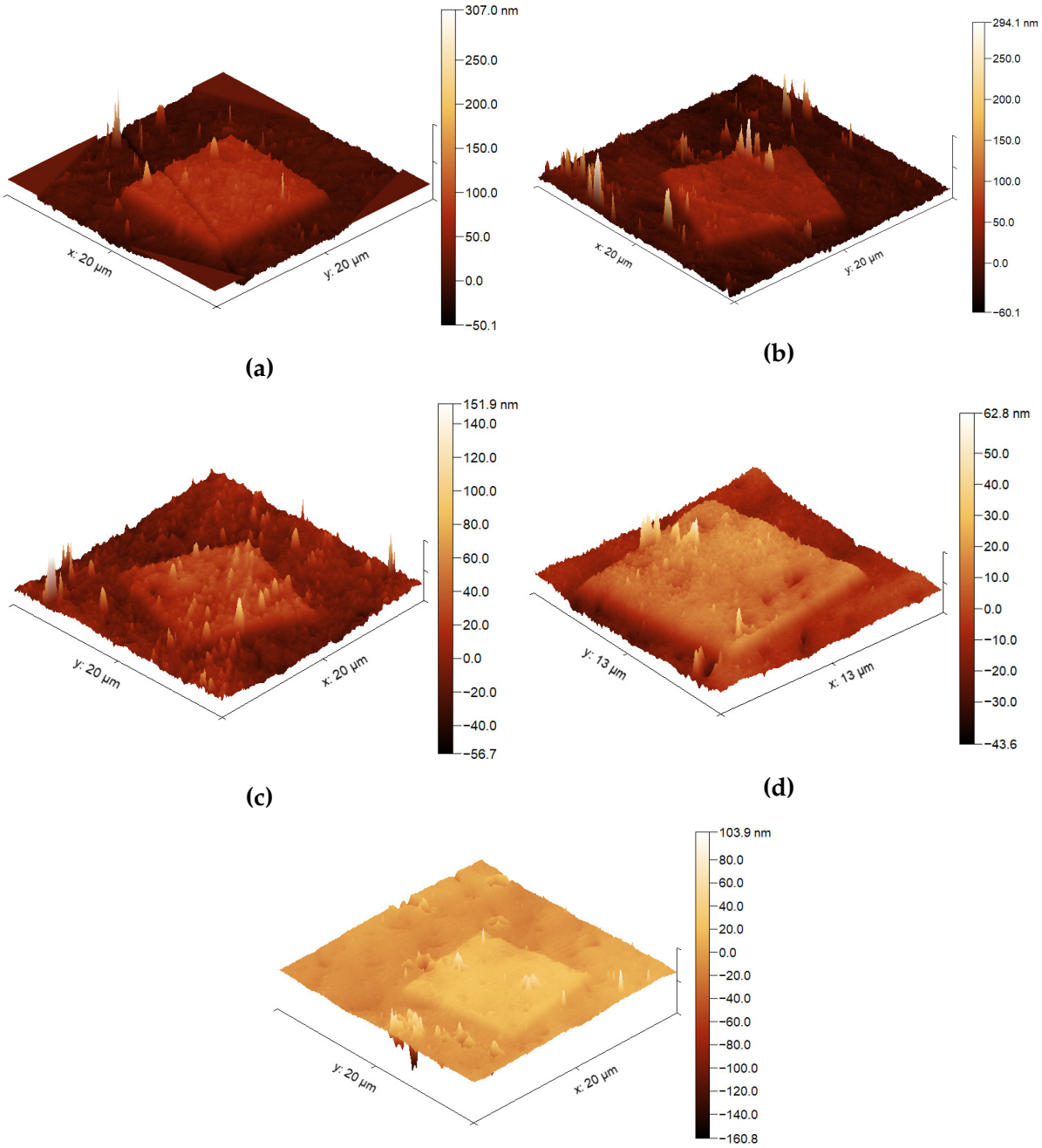

Figure 4.21 Three-dimensional reconstructions of the surface topology of helium implanted regions in NC material gained by AFM measurements. Doses of (a) 1E18, (b) 7.5E17, (c) 5E17, (d) 4E17 and (e) 3E17 Ions/cm^2.

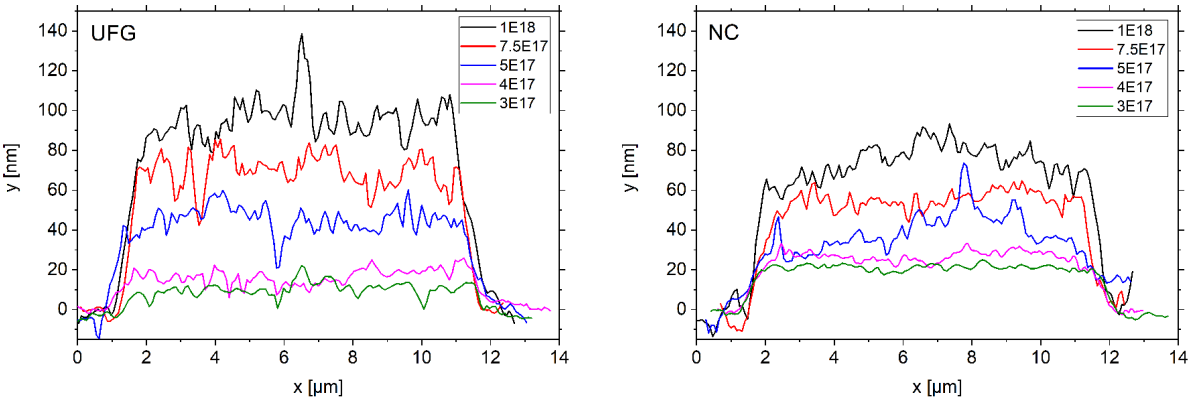

(a) **(b)**

Figure 4.22 Line plots of implanted areas of different helium doses in (a) UFG and (b) NC samples.

The above observations are confirmed by the plots in Figure 4.23. The average swelling height over the helium dose shows different behavior in UFG and NC samples. While the swelling goes rather linear with the dose from 10^{17} to 10^{18} ions/cm^2 in the NC sample, the UFG sample starts off with an exponential growth for low doses before transitioning into a linear trend. The high surface roughness of the implanted area in the UFG material at the highest dose decreases as the dose gets lower, while the roughness in the NC sample stays approximately at the same level.
Figure 4.24 offers a direct comparison of the swelling behavior for both materials.

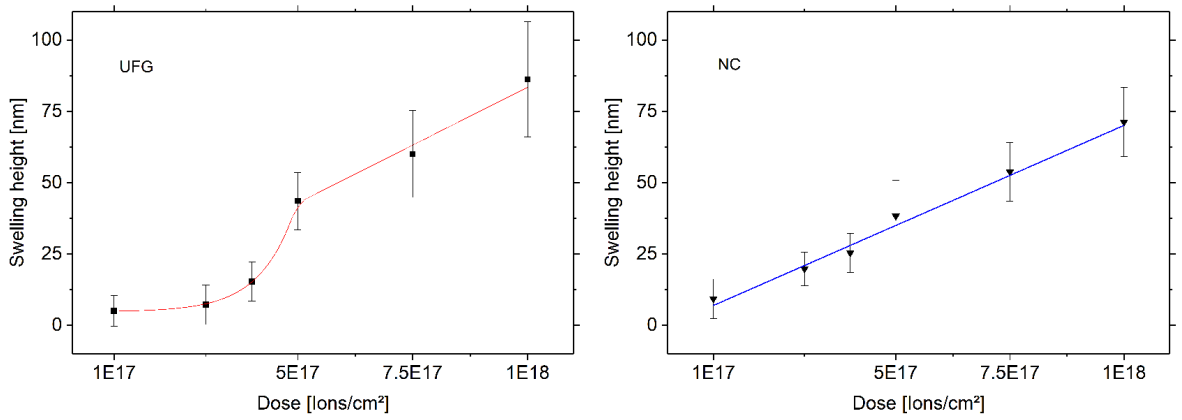

(a) **(b)**

Figure 4.23 Average swelling height of the implanted areas plotted versus helium dose for (a) UFG and (b) NC samples. The lines represent a fit of the trend, the error bars illustrate the surface roughness of the implanted area.

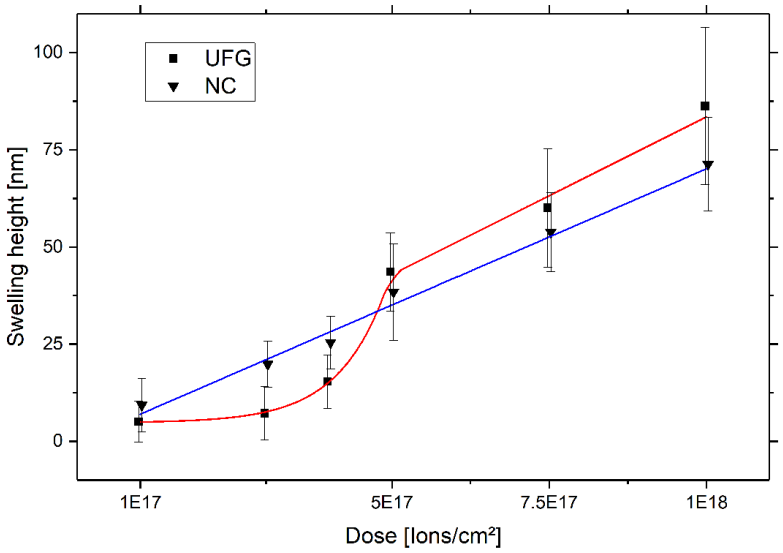

Figure 4.24 Direct comparison of average swelling height for UFG and NC samples. The data points are slightly offset in x-direction to allow a better distinction.

The difference in swelling behavior of UFG and NC material and its underlying mechanisms are discussed in Section 5.3.1. The exact values for swelling height and roughness of the helium implanted regions are listed in Table 4.2.

Table 4.2 Average swelling height and root-mean-squared (RMS) roughness values of implanted areas in UFG and NC material.

	UFG		**NC**	
Dose [ions/cm^2]	Height [nm]	RMS [nm]	Height [nm]	RMS [nm]
1E17	5.09	5.31	9.29	6.92
3E17	7.23	6.91	19.81	5.91
4E17	15.40	6.88	25.42	6.81
5E17	43.61	10.05	38.40	12.41
7.5E17	60.08	15.21	53.80	10.22
1E18	86.23	20.20	71.31	12.09

4.4.2 Mechanical properties

The mechanical properties of unirradiated and helium-ion irradiated materials were investigated using CSM-indentation. For the sake of clarity and for a better way of comparing these indents, the strategy behind analyzing is demonstrated on the hardness and modulus curves of one representative material and dose in Figure 4.25. It is apparent that hardness and modulus of the unirradiated material are higher and less dependent on the indent displacement than in irradiated regions. Surface effects such as the ISE in the unirradiated material or pronounced surface roughness in the irradiated material are also apparent from these data curves. Due to these surface effects all hardness and modulus values were averaged after a displacement of 50 nm as is depicted by the arrow in Figure 4.25. The analysis was carried out until an indentation depth of 200 nm to not get too much influence of the unirradiated material beneath the irradiated layer. The horizontal lines in the graph represent the average values of the respective curves gained by this kind of analysis.

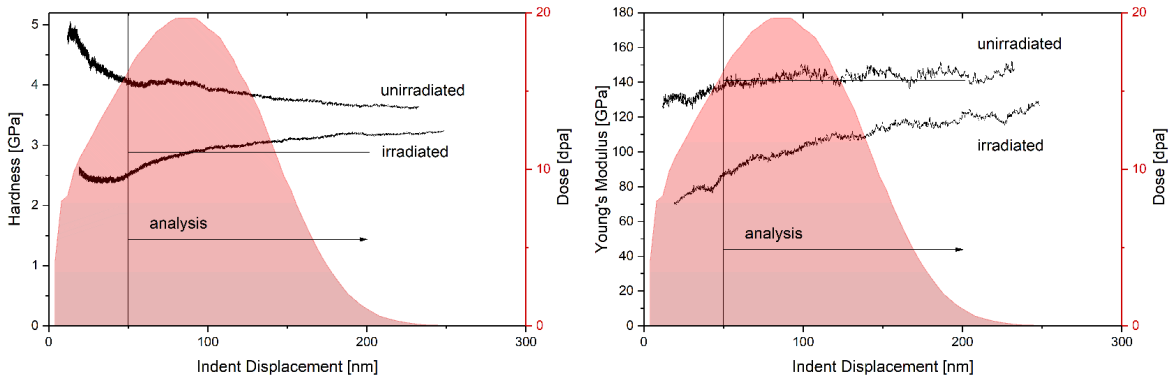

(a) **(b)**

Figure 4.25 Representative CSM curves for (a) hardness and (b) Young's modulus over displacement on UFG material for unirradiated and helium-ion irradiated ($7.5 \cdot 10^{17}$ ions/cm^2) regions. The helium-ion dose in dpa is represented by the red-shaded area.

These average values and their standard deviation within one test series for UFG samples are depicted in Figure 4.26. A slightly higher hardness is observed for low doses before the hardness drops significantly with the helium-ion dose. The Young's modulus, however, shows a continuous decrease from low to high doses with the lowest dose modulus already being slightly lower than the modulus of unirradiated UFG material.

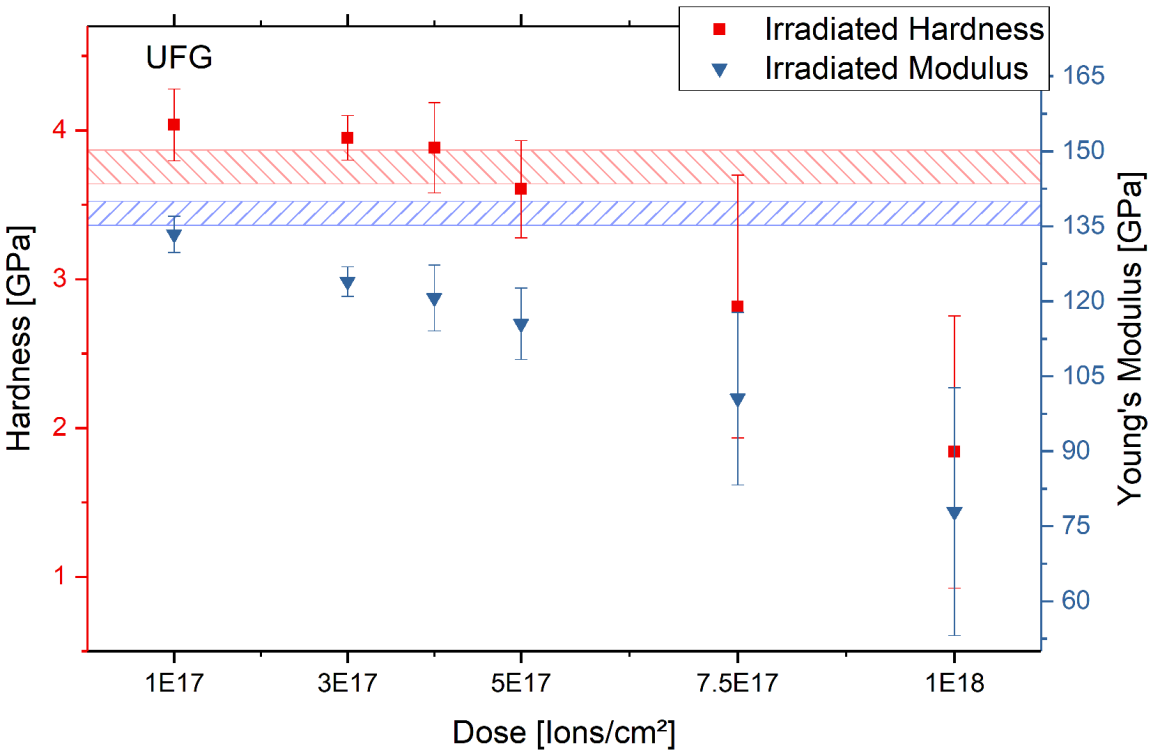

Figure 4.26 Hardness and Young's modulus of irradiated UFG samples as a function of helium-ion dose. The red and blue hatched areas represent the average hardness and modulus of the unirradiated material, respectively.

The same kind of plot for NC samples (Figure 4.27) shows a different behavior. In this material, low doses of helium-ion irradiation already result in lower hardness values with the hardness dropping even further with increasing dose, with the exception of the dose of $5 \cdot 10^{17}$ ions/cm^2, which shows a higher hardness than the trend. The modulus shows a similar behavior. Different parts of the CSM hardness-curve were investigated for the outlying dose. These hardness values are represented by the open symbols in Figure 4.27. It is apparent that analyzing different parts of the CSM curves does not have a lot of influence on the average hardness values. Moreover, as all the separately analyzed values lie within the error bar of the preferred analyzing method, this method is confirmed in its eligibility for easy comparing of CSM-indentation results.

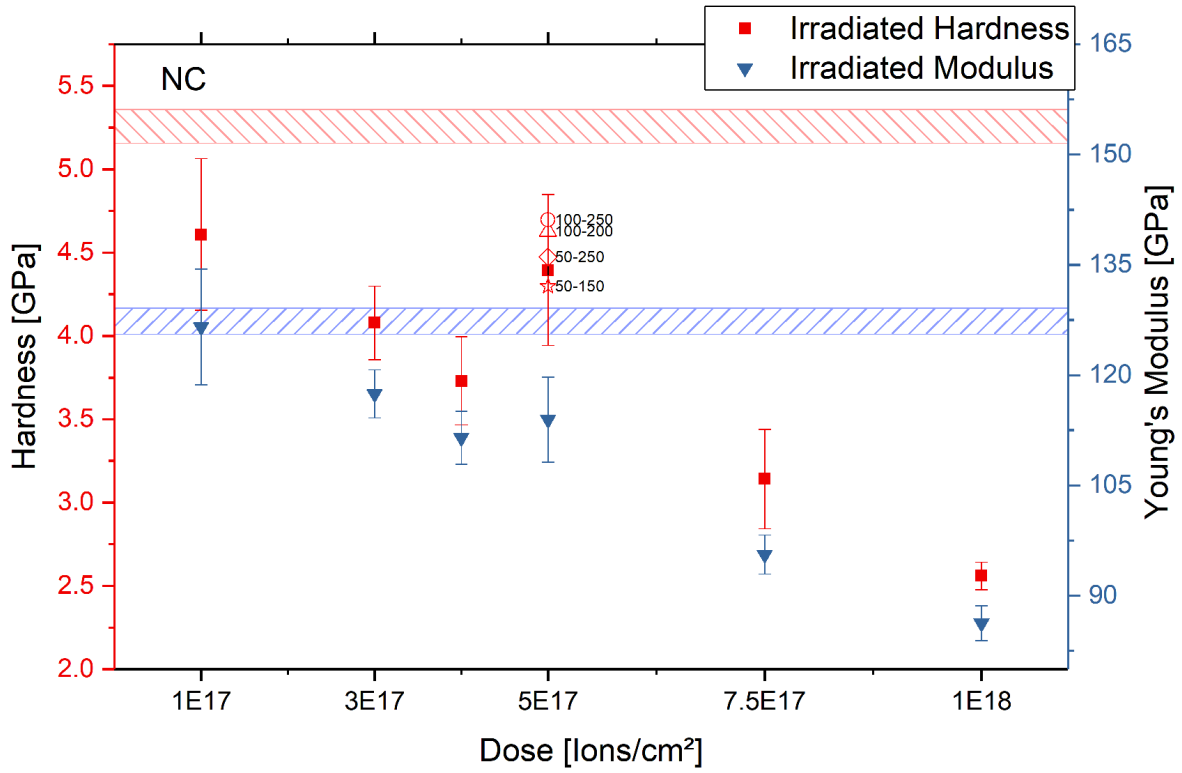

Figure 4.27 Hardness and Young's modulus of irradiated NC samples as a function of helium-ion dose. The red and blue hatched areas represent the average hardness and modulus of the unirradiated material, respectively. The open symbols represent the hardness gained by analyzing different parts of the CSM curve. The numbers next to the open symbols correspond to the analyzed indent depth in nm (compare to Figure 4.25).

5 Discussion

5.1 Sample fabrication

The HIP process was chosen for powder consolidation to achieve a low content of impurities within the material. Unfortunately this was not fully accomplished, as oxides were observed in the SEM investigations after the HIP (see Figure 4.1). It is likely that these oxides already stem from the initial powders and not from the HIP process itself. As they did not influence any later fabrication steps or materials testing, no further investigations regarding the oxide origin and composition were conducted.
The HPT processing worked out without complications and resulted in the majority of the sample volume showing a uniform, single-phased microstructure. This indicates that the three immiscible components, i.e copper, iron and silver, got mechanically alloyed into a supersaturated solid solution.

The DSC measurement yielded a similar behavior than what was determined by Pankhurst et al. [31] for other mechanically alloyed compositions in the Cu-Fe-Ag system. It also indicates that heat treatment at 600°C will get the phases to fully separate again and therefore overcome the metastable state of the material completely, while annealing at 400°C will still leave some forced mixing of the components.
The final microstructure of UFG and NC samples showed good homogeneity throughout the material and the composition is in good agreement with the initial powder mixture. Although the samples showed an indistinguishable microstructure over the better part of the sample volume, later indentations were all performed at a radius of about 2-3 mm to provide the best comparability.
Altogether, the fabrication of bulk samples and precursors for foam processing showed promising results and good reproducibility, making it an easy and effective fabrication route for nanostructured materials.

The foam processing work consisted mainly of finding the right conditions that yield the most uniform microstructure and therefore mechanical properties. Out of the conditions tested within the scope of this thesis, the UFG precursor that underwent

the potentiostatic dealloying at -450 mV for 4 hours showed the most promising results. By adjusting parameters such as dealloying potential, dealloying time, etching solution or temperature, still better results could be achieved. This, however, requires a lot of time and was not in the focus of this thesis.

5.2 Proton irradiation effects on mechanical properties

5.2.1 Bulk material

The indentations directly on the irradiated surface showed unremarkable results, therefore the investigated materials could be claimed to be completely radiation resistant. However, as the additional cross-sectional indents shed more light on the material behavior after irradition, this section will focus on the discussion of these measurements.
First of all it should be mentioned that one should not interpret too much into the properties gained by the outermost indent (the one closest to the surface), as the influence of the embedding compound is very large there. This is confirmed by the still decreasing slope of hardness and modulus at an indentation depth of 1000 nm. The deeper the indent goes, the bigger the plastic zone gets and the more volume of embedding compound is probed.

This effect is especially striking in the UFG material (see Figure 4.15). Indent number 1 shows a strong decrease in hardness with indentation depth. The hardness of indent number 2 shows a less pronounced effect, whereas all other indents show a more or less stable hardness, indicating that they are not probing any embedding compound. However, only analyzing the stable indents still yields an approximately 0.24 GPa or 6.5 % lower hardness than the indents of unirradiated material.
The NC material shows the same behavior with the hardness of irradiated areas being approximately 0.43 GPa or 7.9 % lower than unirradiated areas (see Figures 4.16 and 4.17).

A similar effect of material softening has been observed for annealed and irradiated NC austenitic steel [63]. Heat treatment of such fine-grained materials leads to enhanced dislocation movement. As the high amount of grain boundaries act as sinks for dislocations, nearly dislocation-free grains and an increased hardness are the consequences [64,65]. Introducing lattice defects in such a material through an irradiation treatment will lead to two effects: (i) The majority of radiation-induced defects will annihilate at phase- and grain boundaries. (ii) The remaining defects in

the grain interior can act as dislocation sources, introducing more dislocations in the material and making it softer.
One would expect the NC material to have a less pronounced softening effect, as the higher amount of interfaces would annihilate more radiation-induced defects. However, the opposite case was observed. This can be explained by additional radiation-induced grain growth, which is usually observed at and around the stopping peak. Here the dose-gradient is largest and damaged grains start to grow into neighbouring, undamaged grains [4]. Finer grained materials are more prone to grain growth as they have a bigger drive to reduce their grain boundary energy. Additionally, finer grained materials show a more pronounced softening with increasing grain size according to the famous Hall-Petch relation [66, 67]:

$$\sigma = \sigma_0 + \frac{k_y}{\sqrt{D}} \tag{5.1}$$

with σ representing the strength of the material, σ_0 the strength without grain boundaries, k_y a material constant and D the grain size.
Assuming a total annihilation of radiation-induced defects by the interfaces in NC material, a grain growth of approximately 38 % to an average grain size of 26 nm would be necessary to account for the observed softening by irradiation. Moreover, grain growth also enhances the probability of dislocation sources within a grain. Therefore the slight decrease in hardness in UFG and NC material after proton-irradiation can be explained by a low dislocation density in the annealed material prior to irradiation, the creation of dislocation sources due to radiation and radiation-induced grain growth.

5.2.2 Nanoporous material

The indentation results of NP samples yield a complicated situation in terms of analyzing. As every indent depends heavily on the porosity underneath, extracting radiation-induced changes in hardness is not a straightforward task to do. In the following, the Gibson-Ashby model [46] is applied to accomplish this. As the irradiation treatment should only have little influence on the Young's modulus, Equation 2.9 is used to estimate the porosity under each indent. This porosity is then used in Equation 2.8 to recalculate the hardness of each measurement and extract information on the direct influence of radiation on the hardness of the NP material. Of course this model can only be used as a first approximation, as the equations and their parameters are only valid for macroscopic foams. Additionally, these equations were proposed for foam materials that have the same chemical composition as their

bulk counterparts. As the composition of the here investigated NP material changes due to the dealloying process, this influence on the hardness is not accounted for using this model.
Figure 5.1 shows the hardness values gained by applying this model. The hardness curves still scatter, but less than the original data. The hardness values for irradiated and unirradiated NP material all lie within the same range. It would be bold to claim this material as completely radiation-resistant, considering the large variation in the data. However, it is safe to assume that no distinct radiation hardening effect occurs and that the majority of radiation-induced defects annihilate due to the vast amount of free surface and interfaces in this material.

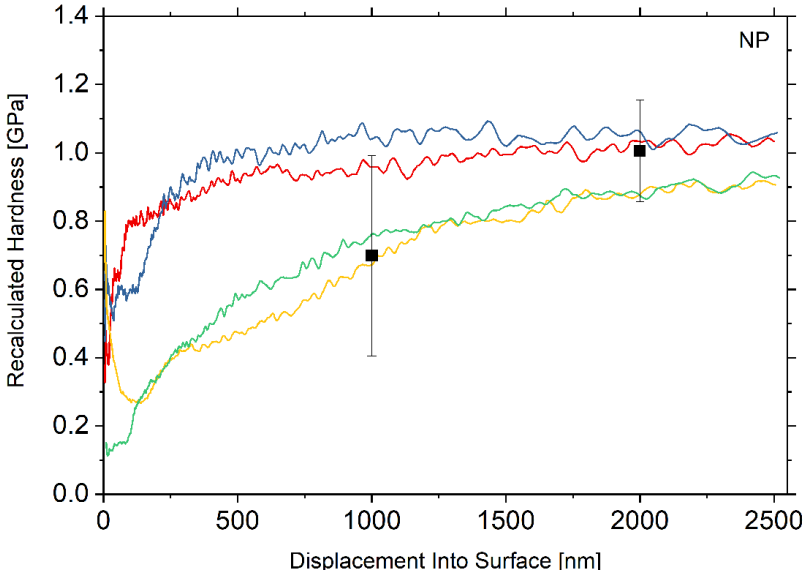

Figure 5.1 Recalculated hardness of the proton-irradiated NP material using the Gibson-Ashby model. The black square symbols represent the average recalculated hardness of unirradiated NP material gained by indentation to 1000 nm and 2000 nm depth.

5.3 Helium effects

5.3.1 Swelling

The swelling behavior of both bulk materials after helium implantation will be discussed in this section. For the sake of simplicity the mechanisms at low doses ($1 \cdot 10^{17}$ to $5 \cdot 10^{17}$ ions/cm^2) will be discussed first, followed by the higher doses ($5 \cdot 10^{17}$ to $1 \cdot 10^{18}$ ions/cm^2).

Low doses

Figures 4.23 and 4.24 illustrate the average swelling height over the helium-ion dose for UFG and NC material. The swelling behavior of UFG samples shows an incubation period and exponential growth at low doses. This can be explained due to the necessity of a certain amount of helium-ions in the grain in order to form bubbles. The more insoluble helium is within the material, the higher is the chance for helium atoms to attract each other and form bubbles. The more the bubbles grow, the easier they attract additional helium-ions, explaining the exponential growth.
In the NC material, however, significant swelling occurs already at lower doses. Two mechanisms are at the root of this behavior: The smaller grain size of about 20 nm results in a much closer spacing of grain- and phase boundaries. This, together with the 5 times higher grain boundary area-to-material volume ratio (~0.1 nm^2/nm^3 compared to ~0.02 nm^2/nm^3 in the UFG material), allows helium-ions in the material to migrate to and along grain boundaries and form helium bubbles there. Another consequence of the smaller grain size in the NC material is a 25 times higher density of triple junctions of grains (~$7.6 \cdot 10^{15}$ m^{-2}). These triple junctions can act as nucleation sites for helium bubbles, resulting in additional heterogeneous nucleation and a higher bubble density.

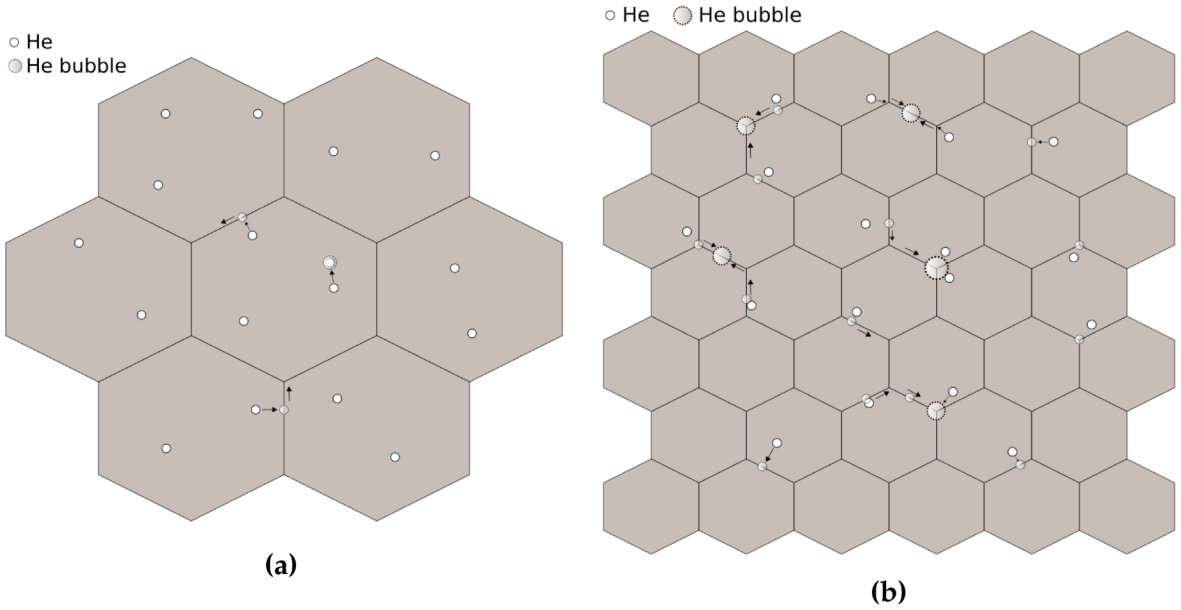

Figure 5.2 Sketch of bubble formation mechanisms in (a) coarse grained and (b) fine grained materials for low helium doses and the same initial helium distribution.

Figure 5.2 illustrates the above mentioned mechanisms for helium accommodation and bubble formation at low doses. It is to be mentioned that, due to demonstrative reasons, the grain size of the finer grained material in this sketch is half as big as in the coarser grained material. Therefore an even bigger difference in helium bubble density is expected between UFG (~100 nm grain size) and NC (~20 nm) material.

High doses

At high doses the increased He-ion density results in a higher probability of helium attracting each other and therefore easier bubble formation. The difference in swelling of the two materials may stem from grain boundaries constraining growth of bubbles nucleated in the grain interior. Furthermore, phase boundaries are known for storing small amounts of helium [17] without nucleating bubbles and also retarding growth of existing bubbles. This is confirmed by the AFM measurements. The UFG material showed a few large blisters with an approximate diameter of 300 nm on the irradiated surface and various smaller blisters with a diameter within 100 nm. The NC material, however, showed even less big blisters and the remaining blisters are considerably smaller than what is observed for UFG material. Thus, the lower swelling in NC material at high doses can be explained by a higher density of interfaces as is illustrated in Figure 5.3.

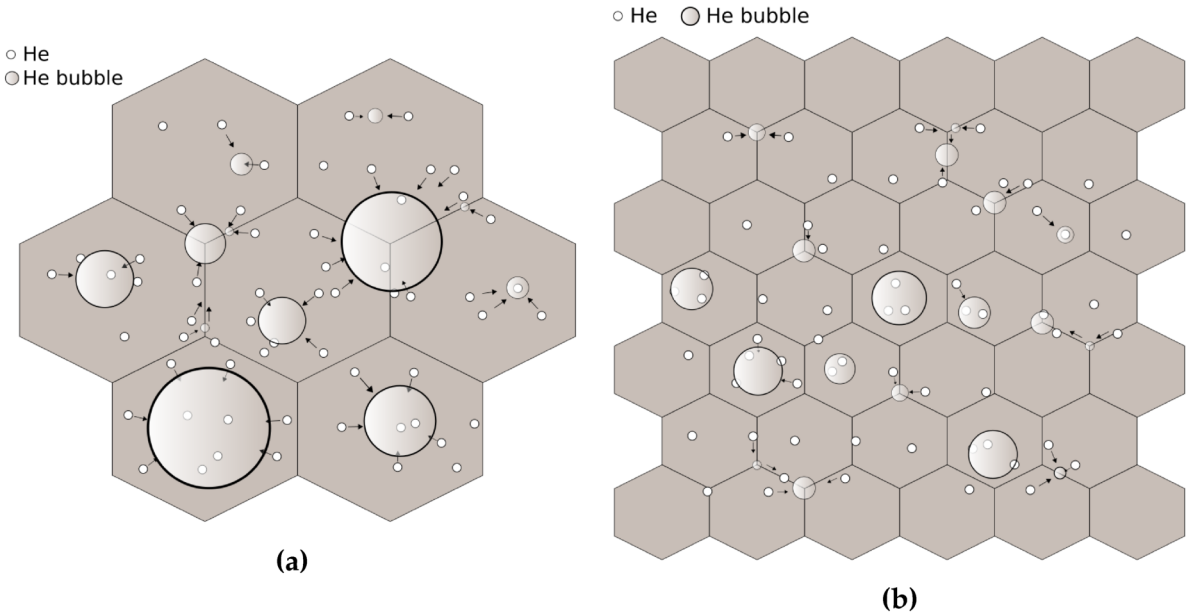

Figure 5.3 Sketch of bubble formation mechanisms in (a) coarse grained and (b) fine grained materials for high helium doses and the same initial helium distribution.

5.3.2 Mechanical properties

The above introduced bubble formation model is in good qualitative agreement with the measured mechanical properties in Figures 4.26 and 4.27.
At low doses the UFG material shows a higher hardness than the unirradiated material. Radiation-induced defects, such as interstitials, frank loops, voids and small bubbles, are the cause of this hardening effect. Helium bubbles grow with increasing dose which eventually results in a porous, foam-like behavior and thus a decrease in hardness. The Young's Modulus decreases continuously with increasing dose, indicating a steady growth of helium bubble size and density. The values for mechanical properties scatter a lot, especially for high doses. This can be explained by the assumption that the helium bubbles are not evenly distributed throughout the irradiated layer. Therefore each indent probes a different volume with more or less bubbles of varying size.
The NC material shows a decrease in hardness already at low doses. This is in good agreement with the proposed bubble formation model. The high amount of grain boundaries in this material allows helium to form bubbles more easily as depicted in Figure 5.2 (b). This again results in a lower hardness and modulus. Both hardness and modulus decrease continuously with increasing dose due to the growing helium bubble population. The cause for the outlying values at $5 \cdot 10^{17}$ ions/cm^2 could not be identified. The experimental setup (indenter, tip, load function) as well as the material sample was the same as for other doses. Hardening mechanisms like radiation-induced segregation or precipitation, triggered by the high dose, can also be ruled out, as the increased hardness was only observed at this specific dose level. Higher dose hardness values lie in good agreement with the low doses. Unfortunately the measurement could not be repeated due to time limitations.

Due to the fact that the plastic zone generated by nanoindentation is larger than the indent depth (see Figure 5.4 (a)), all the mechanical properties gained from irradiated material represent the properties of a composite out of irradiated and unirradiated material. However, only probing the irradiated layer by decreasing the indentation depth is not possible, due to a variety of surface effects influencing the measurement, such as bubble and blister formation, surface roughness or ISE. In order to only extract the mechanical properties of the helium-irradiated zone, a simple volume fraction model was applied.

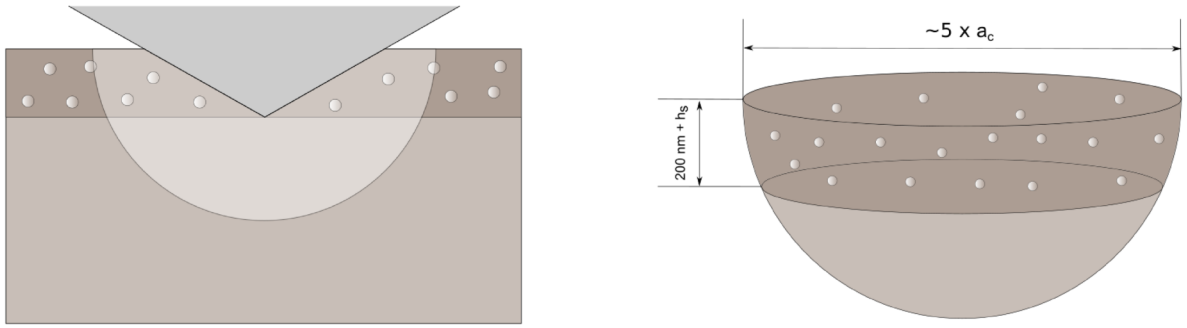

(a) (b)

Figure 5.4 (a) Schematic of the plastic zone generated by indentation of the helium-implanted material. (b) Details and dimensions of the hemispheric plastic zone and the irradiated layer within.

Volume fraction model

The volume fraction model used for analyzing the hardness of the irradiated layer is based on the models proposed by Hosemann et al. [68] and Kareer et al. [69], where the composite hardness at a certain indentation depth H_c is composed of each layer hardness H_i times the probed volume fraction of the layer v_i divided by the whole probed volume:

$$H_c = \frac{\sum H_i \cdot v_i}{\sum v_i} \tag{5.2}$$

The size of the plastic zone generated by nanoindentation is a highly discussed topic [70,71]. The following formula (Johnson's model [70]) allows an approximation of the plastic zone radius c:

$$\left(\frac{c}{a_c}\right)^3 = \frac{1}{3 \cdot \tan\theta} \cdot \frac{E}{\sigma_{ys}} \tag{5.3}$$

where a_c is the contact radius, θ is the semi-apical angle of the indenter (65.27° for a Berkovich indenter), E is the Young's modulus and σ_{ys} is the yield strength of the material. For UFG and NC material the plastic zone size was calculated to be 2.53 and 2.28 times the contact radius, respectively.

The relation between contact radius and contact area can be approximated via:

$$a_c^2 \cdot \pi = A_c \tag{5.4}$$

The contact area A_c can be calculated using the area function and the contact depth (Equations 2.11 through 2.14). Using the equations above, the plastic zone radius for an indentation depth of 200 nm was estimated to be 890 nm in UFG material and 800 nm in NC material.
One has to consider that the helium-irradiated layer does not only consist of the 200 nm deep zone calculated by SRIM (Figure 4.19) but also of the amount of swelled material on top of it (see Table 4.2). Assuming a hemispheric plastic zone and an irradiated layer with a thickness of 200 nm plus the swelling height (Figure 5.4 (b)), the volume fractions of the irradiated and unirradiated layers can be calculated.
Rewriting Equation 5.2 and using the unirradiated hardness values gained by control indents, the hardness of the irradiated layer is calculated by:

$$H_{irr} = \frac{H_c \cdot V_{tot} - H_{unirr} \cdot V_{unirr}}{V_{irr}} \tag{5.5}$$

To avoid surface effects and guarantee a stable hardness value, the composite hardness H_c was taken from an indentation depth of 200 nm.

The calculated hardness values of the helium-affected zone are depicted in Figure 5.5. Naturally, the trend of the values is similar to what is observed in Figures 4.26 and 4.27 and is therefore also explained by the aforementioned helium-bubble formation and growth mechanisms. However, applying the volume fraction model gives a lot of insight on how helium-irradiation directly influences the mechanical properties of the material without the need of higher energetic helium-ions or a more elaborate testing method.
The stress state and plastic zone beneath an indent is of course much more complex than assumed by this model, yet the gained hardness values seem plausible and confirm this model in its eligibility for easy approximation of mechanical properties of differently affected material layers.

The relative difference between helium-irradiated and unirradiated material hardness is depicted in Figure 5.6. The trend is similar to what is discussed above. It is interesting to see that the relative reduction in hardness at a helium-dose of 10^{18} ions/cm^2 is the same in UFG and NC material (about -75 %). This indicates that the helium-bubble population at such high doses is big enough for the microstructure to not have any further influence on bubble formation and growth.

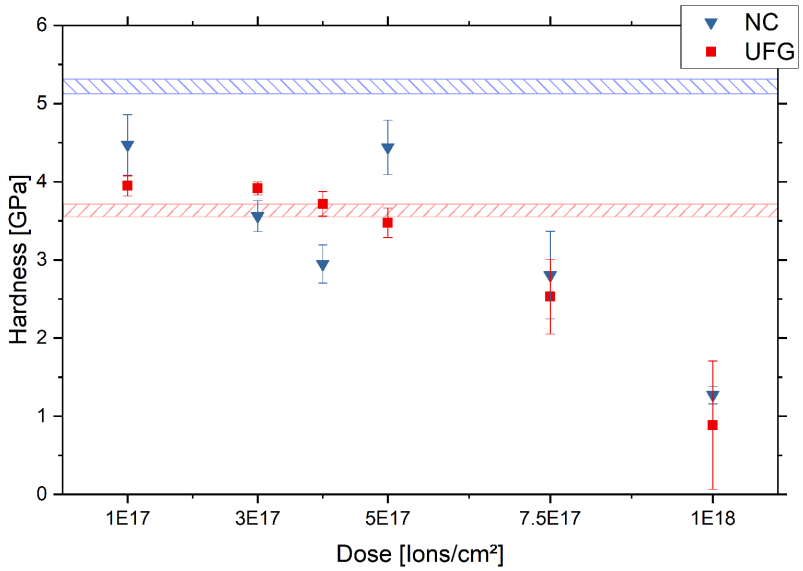

Figure 5.5 Calculated hardness of the helium-implanted layer in UFG and NC material for different helium doses. The red and blue hatched areas represent the average hardness at 200 nm indentation depth for the respective unirradiated material.

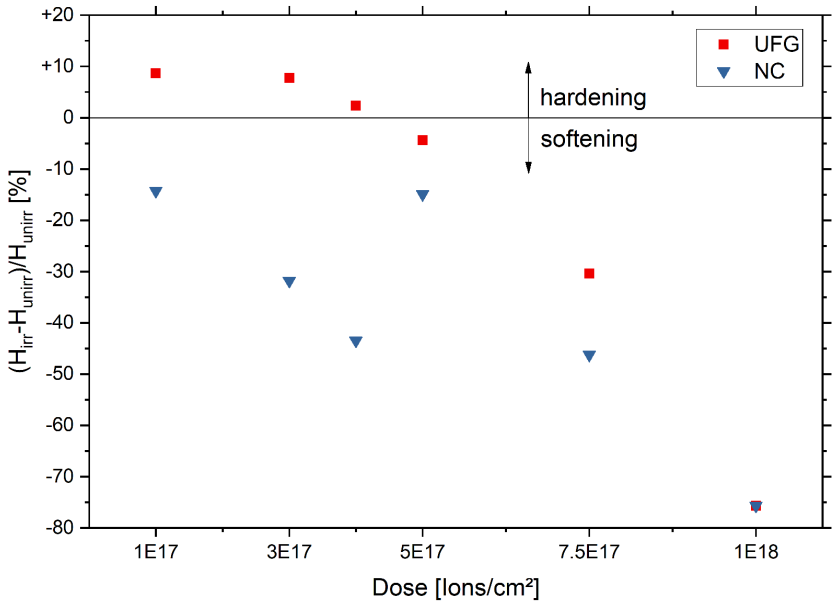

Figure 5.6 Relative difference in hardness of the helium-irradiated and unirradiated UFG and NC material for different helium doses.

6 Summary & Conclusion

In this thesis, nanostructured Cu-Fe-Ag composite materials were fabricated using a solid state route. After mechanical alloying of the components via HPT, a subsequent heat treatment was performed to reach phase separation and adjust the grain size. Material batches with a grain size of about 20 nm (NC material) and 100 nm (UFG material) were produced. Additional NP foam samples were created via potentiostatic dealloying of the UFG material.

The mechanical properties of the differently structured materials were characterized using nanoindentation. All the materials were irradiated with 1 MeV protons. Perpendicular and cross-sectional indentation was performed to investigate the radiation-induced changes in mechanical properties. UFG and NC material showed a slight decrease in hardness after irradiation, which can be attributed to defect annihilation at phase- and grain boundaries, generation of dislocation sources in the grain interior and radiation-induced grain growth.
The measured mechanical properties of the NP material scatter a lot due to inhomogeneity in porosity and composition of the foam. The variation in the measured hardness could be reduced by estimating the porosity under each indent using the measured modulus and the equations proposed by Gibson and Ashby. No notable changes in hardness after proton-irradiation was observed, indicating that the majority of radiation-induced defects is annihilated by the vast amount of interfaces and the goal of creating a completely radiation tolerant material was achieved.

The bulk materials were implanted with 25 keV helium-ions. Swelling measurements using AFM revealed a different behavior for low and high helium doses in the two materials. In the UFG material bubble formation starts out slow for low doses before showing pronounced swelling at high doses. The NC material, however, shows a linear trend in swelling, with more swelling than the UFG material at low doses and less swelling than the UFG material at high doses. This can be attributed to the 5 times higher amount of grain boundaries in the NC material, enhancing helium diffusion and bubble formation at low doses and constraining bubble growth at high doses. CSM-indentations on the helium implanted areas confirmed these observations.

Due to the limited penetration depth of the helium-ions (200 nm) and the plastic zone formed during indentation, probing only the irradiated layer with nanoindentation is not possible. Therefore a volume fraction model was applied to extract the hardness value of the helium-irradiated layer and shed more light on the direct influence of helium-implantation on the mechanical properties. The UFG material experiences a hardening effect for low helium-doses, which can be attributed to formation of radiation-induced defects and small pressurized helium bubbles, acting as obstacles for dislocation movement. Increased bubble size and density at higher doses result in foam-like behavior and, consequently, a distinct drop in hardness. As bubble formation in NC material is enhanced already at low doses, the hardness diminishes continuously with increasing helium-dose.

In conclusion, all investigated nanostructured materials show radiation tolerant properties. This proof-of-principle is an important first step towards novel materials for application in irradiative environments. Studies on and improvement of other application-relevant properties of these materials, such as creep, corrosion or fabrication on a large scale, are still to be made and will strengthen the prospect of deploying nanostructured materials in nuclear or space travel applications.
Another important finding of this work is that helium-bubble formation does not only depend on the helium-dose but also on the microstructure, with coarser grained materials showing advantages in the low dose regime but disadvantages for high helium doses. This interaction of microstructure and helium-irradiation and its consequences on swelling and mechanical properties will be of great interest for designing materials for nuclear fusion applications.

7 References

[1] J.K. Shultis, R.E. Faw, *"Fundamentals of Nuclear Science and Engineering"*, Marcel Dekker Inc., 2002.

[2] P.A. Tipler, G. Mosca, *"Physics for Scientists and Engineers"*, Macmillan, 1994.

[3] K.L. Murty, I. Charit, *"An Introduction to Nuclear Materials: Fundamentals and Application"*, Wiley-VCH Verlag, 2013.

[4] G.S. Was, *"Fundamentals of Radiation Materials Science - Metals and Alloys"*, Springer Berlin Heidelberg, 2007.

[5] J.A. Brinkman, *"Production of atomic displacements by high-energy particles"*, American Journal of Physics, 24: 246-267, 1956.

[6] G.H. Kinchin and R.S. Pease, *"The displacement of atoms in solids by radiation"*, Reports on Progress in Physics, 18: 1, 1955.

[7] D.R. Olander, *"Fundamental Aspects of Nuclear Reactor Fuel Elements"*, Technical Information Center, 1985.

[8] C.R. Barrett, A.S. Tetelman, W.D. Nix, *"The Principles of Engineering Materials"*, Prentice Hall, 1973.

[9] M. Kiritani, *"Story of stacking fault tetrahedra"*, Materials Chemistry and Physics, 50: 133-138, 1997.

[10] B.N. Singh et al., *"Review: Evolution of stacking fault tetrahedra and its role in defect accumulation under cascade damage conditions"*, Journal of Nuclear Materials, 328: 77-87, 2004.

[11] K. Farrell et al., *"Deformation mode maps for tensile deformation of neutron irradiated structural alloys"*, Journal of Nuclear Materials, 335: 471-486, 2004.

[12] B.A. Gurovich et al., *"Assessment of relative contributions from different mechanisms to radiation embrittlement of reactor pressure vessel steels"*, Journal of Nuclear Materials, 246: 91-120, 1997.

[13] P.B. Johnson et al., *"Helium gas bubble lattices in face-centred-cubic metals"*, Nature, 276: 595-596, 1978.

[14] Z.-J. Wang et al., *"Mechanical behavior of copper containing a gas-bubble superlattice"*, Acta Materialia, 121: 78-84, 2016.

[15] K. Farrell et al., *"Modification of radiation damage microstructure by helium"*, Radiation Effects, 78:1-4, 277-295, 1983.

[16] B.N. Singh et al., *"Effect of grain size on void formation during high-energy electron irradiation of austenitic stainless steel"*, Philosophical Magazine, 29: 25-42, 1974.

[17] A. Misra et al., *"The Radiation Damage Tolerance of Ultra-High Strength Nanolayered Composites"*, JOM, 59: 62-65, 2007.

[18] E.G. Fu et al., *"Surface effects on the radiation response of nanoporous Au foams"*, Applied Physics Letters, 101: 191607, 2012.

[19] E.M. Bringa et al., *"Are Nanoporous Materials Radiation Resistant?"*, Nano Letters, 12: 3351-3355, 2012.

[20] I.J. Beyerlein et al., *"Radiation damage tolerant nanomaterials"*, Materials Today, 16: 443-449, 2013.

[21] W. Han et al., *"Design of Radiation Tolerant Materials Via Interface Engineering"*, Advanced Materials, 25: 6975-6979, 2013.

[22] C. Sun et al., *"In situ study of defect migration kinetics in nanoporous Ag with enhanced radiation tolerance"*, Scientific Reports, 4: 3737, 2014.

[23] Y. Ding et al., *"Metallic Mesoporous Nanocomposites for Electrocatalysis"*, Journal of the American Chemical Society, 126: 6876-6877, 2004.

[24] K. Bonroy et al., *"Realization and Characterization of Porous Gold for Increased Protein Coverage on Acoustic Sensors"*, Analytical Chemistry, 76: 4299-4306, 2004.

[25] D. Kramer et al., *"Surface-Stress Induced Macroscopic Bending of Nanoporous Gold Cantilevers"*, Nano Letters, 4: 793-796, 2004.

[26] P.S. Liu et al., *"Review Functional materials of porous metals made by P/M, electroplating and some other techniques"*, Journal of Materials Science, 36: 5059-5072, 2001.

[27] MTDATA Calculations, http://resource.npl.co.uk/mtdata/phdiagrams/cufe.htm, National Physical Laboratory [Accessed 6 Nov 2017]

[28] MTDATA Calculations, http://resource.npl.co.uk/mtdata/phdiagrams/agfe.htm, National Physical Laboratory [Accessed 6 Nov 2017]

[29] G. Gottstein, *"Physical Foundations of Materials Science"*, Springer, 2004.

[30] N.S. Cohen et al., *"Investigation of the ternary phase diagram of mechanically alloyed FeCuAg"*, Journal of Physics: Condensed Matter, 9: 3259-3276, 1997.

[31] Q.A. Pankhurst et al., *"Thermal analysis of metastable Fe-Cu-Ag prepared by mechanical alloying"*, Journal of Physics: Condensed Matter, 10: 1665- 1676, 1998.

[32] R.Z. Valiev et al., *"Bulk nanostructured materials from severe plastic deformation"*, Progress in Materials Science, 45: 103-189, 2000.

[33] N. Tsuji et al., *"ARB (Accumulative Roll-Bonding) and other new Techniques to Produce Bulk Ultrafine Grained Materials"*, Advanced Engineering Materials, 5: 338-344, 2003.

[34] R. Pippan et al., *"Advantages and limitations of HPT: a review"*, Materials Science Forum, 584-586: 16-21, 2008.

[35] V. Viswanathan et al., *"Challenges and advances in nanocomposite processing techniques"*, Materials Science and Engineering R, 54: 121-285, 2006.

[36] X. Sauvage et al., *"Mechanical alloying of Cu and Fe induced by severe plastic deformation of a Cu-Fe composite"*, Acta Materialia, 53: 2127-2135, 2005.

[37] X. Sauvage et al., *"Nanoscaled structure of a Cu-Fe composite processed by high-pressure torsion"*, Materials Science and Engineering: A, 410-411: 345-347, 2005.

[38] A. Bachmeier, R. Pippan, *"Generation of metallic nanocomposites by severe plastic deformation"*, International Materials Reviews, 58:1, 41-62, 2013.

[39] A. Kumar et al., *"Mechanical alloying and properties of immiscible Cu-20 wt.% Mo alloy"*, Journal of Alloys and Compounds, 647: 1040-1047, 2015.

[40] N. Ibrahim et al., *"Mechanical alloying via high-pressure torsion of the immiscible $Cu_{50}Ta_{50}$ system"*, Materials Science and Engineering A, 685: 19-30, 2017.

[41] M. Kreuzeder et al., *"Fabrication and thermo-mechanical behavior of nanoporous copper"*, Journal of Materials Science, 50: 634-643, 2015.

[42] A. Leitner et al.,*"Interface dominated mechanical properties of ultra-fine grained and nanoporous Au at elevated temperatures"* , Acta Materialia, 121: 104-116, 2016.

[43] P.C. Oliveira et al., *"Leaching studies for metals recovery from printed circuit boards scrap"*, Electronics & Battery Recycling '09, 2009.

[44] P. Atkins, J. de Paula, *"Physical Chemistry"*, Oxford University Press, W.H. Freeman and Company, Eight Edition, 2006.

[45] C.G. Zoski, *"Handbook of Electrochemistry"*, Elsevier B.V., 2007.

[46] L.J. Gibson, M.F. Ashby, *"Cellular Solids: Structure and Properties"*, Cambridge University Press, Second Edition, 1999.

[47] A.M. Hodge et al., *"Scaling equation for yield strength of nanoporous open-cell foams"*, Acta Materialia, 55: 1343-1349, 2007.

[48] N.J. Briot et al., *"Mechanical properties of bulk single crystalline nanoporous gold investigated by millimetre-scale tension and compression testing"*, Philosophical Magazine, 94: 847-866, 2014.

[49] J. Biener et al., *"Nanoporous Au: A high yield strength material"*, Journal of Applied Physics, 97: 024301, 2005.

[50] O.B. Olurin et al., *"Deformation and fracture of aluminium foams"*, Materials Science and Engineering, A291: 136-146, 2000.

[51] L. Luehrs et al., *"Elastic and plastic Poisson's ratios of nanoporous gold"*, Scripta Materialia, 110: 65-69, 2016.

[52] G.S. Was et al., *"Emulation of neutron irradiation effects with protons: validation of principle"*, Journal of Nuclear Materials, 300: 198-216, 2002.

[53] D. Kiener et al., *"Application of small-scale testing for investigation of ion-beam-irradiated materials"*, Journal of Materials Research, 27: 2724-2736, 2012.

[54] P. Hosemann et al., *"Small scale mechanical testing of irradiated materials"*, Journal of Materials Research, 30: 1-15, 2015.

[55] A.C. Fischer-Cripps, *"Nanoindentation"*, Springer, Third Edition, 2011.

[56] W.C. Oliver, G.M. Pharr, *"An improved technique for determining hardness and elastic modulus using load and displacement sensing indentation experiments"*, Journal of Materials Research, 7: 1564-1583, 1992.

[57] I.N. Sneddon, *"The relation between load and penetration in the axisymmetric boussinesq problem for a punch of arbitrary profile"*, International Journal of Engineering Science, 3: 47-57, 1965.

[58] X. Li, B. Bhushan, *"A review of nanoindentation continuous stiffness measurement technique and its applications"*, Materials Characterization, 48: 11-36, 2002.

[59] V. Maier, K. Durst, *"Advanced Nanoindentation testing for studying strain-rate sensitivity and activation volume"*, Journal of Materials, 69: 2246-2255, 2017.

[60] W.D. Nix, H. Gao, *"Indentation size effects in crystalline materials"*, Journal of the Mechanics and Physics of Solids, 46: 411-424, 1998.

[61] J.F. Ziegler, J.P. Biersack, U. Littmark, *"The Stopping Range of Ions in Matter"*, Pergamon Press, New York, 1985.

[62] N.M. Everitt et al., *"High temperature nanoindentation - the importance of isothermal contact"*, Philosophical Magazine, 91: 1221-1244, 2011.

[63] M. Alfreider, *"The influence of deformation and proton-irradiation on the mechanical behaviour in nano-crystalline stainless steels"*, Master Thesis, 2017.

[64] X. Huang et al., *"Hardening by annealing and softening by deformation in nanostructured metals"*, Science, 312: 249-251, 2006.

[65] O. Renk et al., *"Increasing the strength of nanocrystalline steels by annealing: Is segregation necessary?"*, Scripta Materialia, 95: 27-30, 2015.

[66] E.O. Hall, *"The deformation and ageing of mild steel: III Discussion of results"*, Proceedings of the Physical Society B, 64: 747-753, 1951.

[67] R.J. Petch, *"The cleavage strength of polycrystals"*, Journal of the Iron and Steel Institute, 174: 25-28, 1953.

[68] P. Hosemann et al., *"Issues to consider using nano indentation on shallow ion beam irradiated materials"*, Journal of Nuclear Materials, 425: 136-139, 2012.

[69] A. Kareer et al., *"An analytical method to extract irradiation hardening from nanoindentation hardness-depth curves"*, Journal of Nuclear Materials, 498: 274-281, 2018.

[70] K.L. Johnson, *"The correlation of indentation experiments"*, Jounral of the Mechanics and Physics in Solids, 18: 115-126, 1970.

[71] M. Mata et al., *"The plastic zone size in indentation experiments: The analogy with the expansion of a spherical cavity"*, International Journal of Solids and Structures, 43: 5994-6013, 2006.